RWTH Aachen University

Scattering off Single-Site Impurities in Graphene

Bachelor's Thesis

Sinan Blanck

under the supervision of
Prof. Dr. Fabian Hassler

September 21, 2026

Abstract

This thesis studies the problem of low-energy scattering off impurities in tight-binding graphene. We linearise the tight-binding Hamiltonian for low energies around the two Dirac points. We then use the Lippmann-Schwinger equation to obtain the scattering states and calculate the scattering amplitudes for single-site impurities. For this, we use the Green's function approximated for a continuum and compare it to a numerical evaluation. We find good agreement between the analytical and numerical results for the far field. Furthermore, we determine the exact analytical solution for the Green's function at zero distance. We calculate the scattering amplitudes, determine the scattering cross section and find that it is isotropic and independent of the valley. From this, we estimate the conductivity for a density of vacancies. Further, we analyse an impurity within a graphene quantum dot using degenerate perturbation theory. We find that the impurity lifts the degeneracy and leaves one unshifted equal-weight superposition for each pair of states at different Dirac points.

Contents

Abstract **i**

1 Introduction **1**

2 Model and conventions **3**

2.1 Lattice geometry 3

2.2 Tight-binding Hamiltonian and structure factor 3

2.3 Dirac points and linearisation 5

3 The Dirac Green's function **6**

3.1 Scattering problem and Lippmann-Schwinger equation 6

3.2 Reduction to a scalar problem and Fourier transform 7

3.3 Contour deformation and residue 7

3.4 The matrix Green's function 8

4 Numerical evaluation of the lattice Green's function **10**

4.1 Integral representation of the Green's function 10

4.2 The analytical zero solution 11

4.3 Numerical validation against the Dirac approximation 12

5 Solution of the Lippmann-Schwinger equation for a single impurity **13**

5.1 Lippmann-Schwinger equation and self-consistency condition 13

5.2 Incoming plane wave 14

5.3 Scattered wave and scattering amplitude 14

5.4 Scattering cross section 15

5.5 Optical theorem 16

5.6 Conductivity for a density of impurities 17

5.7 Conductivity at low energies 18

5.8 Comparison with other results 18

6 Quantum dot formalism and eigenstates 21

6.1 The modified Hamiltonian 21

6.2 Conserved angular momentum 22

6.3 Eigenstates of the angular momentum operator 22

6.4 The radial functions 23

6.5 Spectrum of the Hamiltonian 24

6.6 Perturbation theory for an impurity 25

7 Conclusion and outlook 28

A Deriving the relation to the Horiguchi result 30

A.1 Ansatz for G_0 30

A.2 Rewriting $|f(\boldsymbol{k})|^2$ and determining the integral boundaries 30

A.3 Transforming the integral and finding the expression 31

B Comparison to the Basko result 33

Bibliography 35

Chapter 1

Introduction

In many parts of physics, the study of graphene has become a central topic. This is due to graphene being one of the true two-dimensional materials [1]. It is a two-dimensional honeycomb lattice with two atoms per unit cell. Today, its electronic properties are well studied [2]. At low energies, the dispersion is linear around the two Dirac points, and the electrons are described by a Dirac Hamiltonian. This makes the low-energy regime of graphene accessible to analytical methods, and this regime will be the focus of this thesis.

However, in real samples, impurities are always present. They scatter the electrons and thus determine properties like the conductivity [3, 4]. The simplest model for such a defect is a single-site impurity, which we will describe by an additional short-range potential of strength V_0 on one lattice site. In the limit $V_0 \to \infty$, no state is allowed on that site [5]. After studying the effect of a single impurity, one can proceed to a density of impurities.

In this thesis, we study the low-energy scattering off a single impurity in graphene analytically. The aim is to use the Lippmann-Schwinger equation to calculate the scattering amplitude, the cross section and finally the conductivity for a density of vacancies. Afterwards, we consider an impurity in a graphene quantum dot, where the spectrum is discrete.

An existing result for the scattering amplitude of a single impurity in graphene was derived by Basko [6]. However, the Green's function at zero distance entering this result contains a constant that was determined by numerical integration over the Brillouin zone. In this thesis, we derive an analytical expression for the Green's function at zero distance and combine it with the approximate far-field solution at low energy.

The thesis is structured as follows. In Chapter 2, we introduce the tight-binding model for the honeycomb lattice and linearise it around the Dirac points. In Chapter 3, we introduce the scattering problem with the Lippmann-Schwinger equation, for which we derive an analytical far-field result for the Green's function at low energies. In Chapter 4, this Green's function is compared to a numerical evaluation of the exact Green's function of the tight-binding model. Additionally, the exact analytical value at zero distance is derived. Combining the approximate far-field form and the exact zero-distance form, we solve the Lippmann-Schwinger equation for a single impurity in Chapter 5. This yields the scattering amplitude, and we calculate the cross section, compare them to the result of Basko [6], verify them with the optical theorem and estimate the conductivity for a density of vacancies. This conductivity is then compared to

other theoretical results and to a measurement on ion-irradiated graphene. In Chapter 6, we consider a circular quantum dot defined by a mass term, determine its eigenstates and discuss the effect of an impurity with degenerate perturbation theory.

Chapter 2

Model and conventions

This chapter introduces the model for the graphene lattice and establishes the conventions used throughout this thesis. The graphene lattice is a honeycomb lattice with two sublattices A and B. In the tight-binding approximation, the Hamiltonian describes the hopping of electrons between neighbouring sites [2, 7]. Here, we only consider hopping between nearest neighbours. The on-site energies are equal on A and B, so they can be set to zero. This only shifts the energy but simplifies the expressions. Using this model, the eigenvalues and eigenstates will be determined, and an approximation for small energies will be derived.

2.1 Lattice geometry

Firstly, we introduce some of the conventions used in the following. The Bravais vectors of the honeycomb lattice are chosen to be

$$\boldsymbol{a}_1 = \frac{a}{2}(3, \sqrt{3}), \qquad \boldsymbol{a}_2 = \frac{a}{2}(3, -\sqrt{3}). \tag{2.1}$$

The three vectors connecting the nearest neighbours follow as

$$\boldsymbol{\delta}_1 = a(1, 0), \qquad \boldsymbol{\delta}_2 = a\left(-\tfrac{1}{2}, -\tfrac{\sqrt{3}}{2}\right), \qquad \boldsymbol{\delta}_3 = a\left(-\tfrac{1}{2}, +\tfrac{\sqrt{3}}{2}\right), \tag{2.2}$$

as shown in Fig. 2.1. The distance between nearest neighbours is denoted by $a = |\boldsymbol{\delta}_i|$. The area of the unit cell is $A_{\text{cell}} = 3\sqrt{3}a^2/2$.

The reciprocal basis to $(\boldsymbol{a}_1, \boldsymbol{a}_2)$ consists of the vectors $(\boldsymbol{b}_1, \boldsymbol{b}_2)$ fulfilling $\boldsymbol{a}_i \cdot \boldsymbol{b}_j = 2\pi\delta_{ij}$. They are calculated to be

$$\boldsymbol{b}_1 = \frac{2\pi}{3a}(1, \sqrt{3}), \qquad \boldsymbol{b}_2 = \frac{2\pi}{3a}(1, -\sqrt{3}). \tag{2.3}$$

2.2 Tight-binding Hamiltonian and structure factor

The tight-binding Hamiltonian for the honeycomb lattice with nearest-neighbour hopping t is

$$\mathcal{H} = -t \sum_{\langle i,j \rangle} |i\rangle\langle j| + \text{h.c.}, \tag{2.4}$$

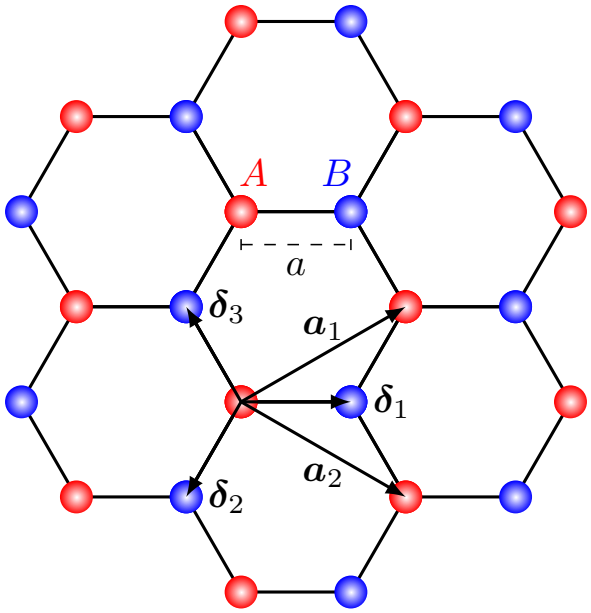


Figure 2.1: Honeycomb lattice with Bravais vectors $\boldsymbol{a}_1$ and $\boldsymbol{a}_2$, and nearest-neighbour vectors $\boldsymbol{\delta}_1$, $\boldsymbol{\delta}_2$ and $\boldsymbol{\delta}_3$.

where $|i\rangle$ is the state of an electron on site i and the sum runs over nearest-neighbour pairs $\langle i,j\rangle$. Ignoring every other interaction is part of the tight-binding approach.

We use the Fourier transform $|i\rangle = 1/\sqrt{NM}\sum_{\boldsymbol{k}} \mathrm{e}^{\mathrm{i}\boldsymbol{k}\cdot\boldsymbol{r}_i}|\boldsymbol{k}\rangle$ and $1/(NM)\sum_i \mathrm{e}^{\mathrm{i}(\boldsymbol{k}-\boldsymbol{k}')\cdot\boldsymbol{r}_i} = \delta_{\boldsymbol{k},\boldsymbol{k}'}$, where N and M are the numbers of unit cells in each direction, to write the Hamiltonian in momentum space [8]. We find

$$\mathcal{H} = -t\sum_{\boldsymbol{k}}\sum_{\boldsymbol{\delta}} \mathrm{e}^{-\mathrm{i}\boldsymbol{k}\cdot\boldsymbol{\delta}}\,|\boldsymbol{k},A\rangle\langle\boldsymbol{k},B| + \text{h.c.} = -t\sum_{\boldsymbol{k}} \begin{pmatrix} 0 & f(\boldsymbol{k}) \\ f^*(\boldsymbol{k}) & 0 \end{pmatrix} |\boldsymbol{k}\rangle\langle\boldsymbol{k}|, \tag{2.5}$$

where $f(\boldsymbol{k}) = \sum_{\boldsymbol{\delta}} \mathrm{e}^{-\mathrm{i}\boldsymbol{k}\cdot\boldsymbol{\delta}}$ is the structure factor and the sum runs over $\boldsymbol{\delta}_1, \boldsymbol{\delta}_2, \boldsymbol{\delta}_3$ of Eq. (2.2). Carrying out the sum gives

$$f(\boldsymbol{k}) = \mathrm{e}^{-\mathrm{i}ak_x}\left(1 + 2\,\mathrm{e}^{\mathrm{i}\frac{3}{2}ak_x}\cos\left(\frac{\sqrt{3}a}{2}\,k_y\right)\right). \tag{2.6}$$

The 2×2 structure of the Hamiltonian Eq. (2.5) represents the two sublattices A and B of the honeycomb lattice.

The eigenvalues and eigenvectors of the block matrix Eq. (2.5) are

$$E(\boldsymbol{k}) = \pm t\,|f(\boldsymbol{k})|\,, \qquad \chi_{\boldsymbol{k},\pm} = \frac{1}{\sqrt{2}}\begin{pmatrix} 1 \\ \pm\mathrm{e}^{-\mathrm{i}\arg(-tf(\boldsymbol{k}))} \end{pmatrix}. \tag{2.7}$$

2.3 Dirac points and linearisation

The band energy is proportional to the structure factor Eq. (2.6). It vanishes at the two Dirac points $\boldsymbol{K}$ and $\boldsymbol{K}'$ in the first Brillouin zone, which are given by

$$\boldsymbol{K} = \left(0, \frac{4\pi}{3\sqrt{3}a}\right), \qquad \boldsymbol{K}' = \left(0, -\frac{4\pi}{3\sqrt{3}a}\right). \tag{2.8}$$

We introduce the valley index $\tau = +1$ for $\boldsymbol{K}$ and $\tau = -1$ for $\boldsymbol{K}'$. It will serve both as an index and as a sign factor of the valley-dependent results. Setting $\boldsymbol{k} \to \boldsymbol{K}^\tau + \boldsymbol{q}$ and expanding $f(\boldsymbol{k})$ to linear order in $\boldsymbol{q}$ yields

$$\begin{pmatrix} 0 & -tf(\boldsymbol{k}) \\ -tf^*(\boldsymbol{k}) & 0 \end{pmatrix} \longrightarrow \mathcal{H}^\tau(\boldsymbol{q}) = \begin{pmatrix} 0 & v(\tau q_y + \mathrm{i}q_x) \\ v(\tau q_y - \mathrm{i}q_x) & 0 \end{pmatrix}, \tag{2.9}$$

with $v = 3at/2$. We call this the Dirac approximation and $\mathcal{H}^\tau(\boldsymbol{q})$ the Dirac Hamiltonian.

It is worth noting that, in this limit, $\arg(-tf(\boldsymbol{k}))$ is given by

$$\arg(\tau q_y + \mathrm{i}q_x) = \frac{\pi}{2} - \tau\varphi, \tag{2.10}$$

where φ is the polar angle of $\boldsymbol{q}$.

This limit is valid for $a|\boldsymbol{q}| \ll 1$ (equivalently $|E| \ll t$) and thus constitutes a low-energy approximation to the full tight-binding model. In this limit, the dispersion is the linear, isotropic Dirac cone $E(\boldsymbol{q}) = \pm v|\boldsymbol{q}|$ [2]. The analytical results derived in the following chapters rest on this linearisation and are a valid analytical description only in this low-energy regime with corrections of order $(a|\boldsymbol{q}|)^2$.

With this Dirac Hamiltonian, the basic framework is established. The next chapters will use this model to derive results for a single impurity in plain graphene and in a graphene quantum dot.

Chapter 3

The Dirac Green's function

For a sufficiently large system, the eigenvalues of the Hamiltonian Eq. (2.5) form a continuum, and the sum over $\boldsymbol{k}$ can be replaced by an integral. In this limit, scattering problems are solved using the Lippmann-Schwinger equation. For graphene, which we treat as an infinitely large sheet, this is the appropriate limit. In this chapter, we derive the Green's function of the Dirac Hamiltonian.

3.1 Scattering problem and Lippmann-Schwinger equation

At fixed energy $E(\boldsymbol{k})$, we split

$$\mathcal{H} = \mathcal{H}_0 + V \qquad \Longrightarrow \qquad (E - \mathcal{H}_0)\,\psi = V\psi, \tag{3.1}$$

with the unperturbed Hamiltonian $\mathcal{H}_0$, the impurity potential V and an eigenfunction ψ of the full Hamiltonian $\mathcal{H}$ at the energy $E = E(\boldsymbol{k})$ of the incoming wave. For elastic scattering, this can be solved by the Lippmann-Schwinger equation [9]

$$\psi(\boldsymbol{r}) = \psi_{\text{in}}(\boldsymbol{r}) + \sum_i G_0(\boldsymbol{r} - \boldsymbol{r}_i; E)\, V(\boldsymbol{r}_i)\, \psi(\boldsymbol{r}_i), \tag{3.2}$$

with the matrix Green's function defined by [10]

$$(E - \mathcal{H}_0)\, G_0(\boldsymbol{r} - \boldsymbol{r}_i; E) = \delta_{\boldsymbol{r}\boldsymbol{r}_i}\, \mathbb{1}_2. \tag{3.3}$$

To ensure the correct solution, the Green's function is defined as the limit

$$G_0(\boldsymbol{r} - \boldsymbol{r}_i; E) = \lim_{\varepsilon \to 0^+} G_0(\boldsymbol{r} - \boldsymbol{r}_i; E + \mathrm{i}\varepsilon), \tag{3.4}$$

which for $\varepsilon > 0$ selects the outgoing wave [10] and will be used in Eq. (3.11). This Green's function is derived in the following sections.

3.2 Reduction to a scalar problem and Fourier transform

We now want to transform the problem into a more manageable form. Without reference to the position basis, we write $G_0(E) = (E - \mathcal{H}_0)^{-1}$ and find

$$G_0(E) = (E - \mathcal{H}_0)^{-1} = (E + \mathcal{H}_0)\left(E^2 - \mathcal{H}_0^2\right)^{-1}. \tag{3.5}$$

The square of Eq. (2.9) is proportional to the identity, $\mathcal{H}_0^2 = v^2 q^2 \mathbb{1}_2$, where $q = |\boldsymbol{q}|$. Now the inverse in Eq. (3.5) is a scalar problem. Defining g_0 by $\left(E^2 - \mathcal{H}_0^2\right)^{-1} = g_0 \mathbb{1}_2$ yields, in $\boldsymbol{k}$ space,

$$g_0(\boldsymbol{q}) = \frac{\gamma}{k_E^2 - q^2}, \tag{3.6}$$

with the abbreviations $k_E^2 = E^2/v^2$ and $\gamma = 1/v^2$.

Back in position space, we have

$$g_0(\boldsymbol{r}) = \frac{A_{\text{cell}}\gamma}{(2\pi)^2} \int \mathrm{d}^2 q \, \frac{\mathrm{e}^{\mathrm{i}\boldsymbol{q}\cdot\boldsymbol{r}}}{k_E^2 - q^2} = \frac{A_{\text{cell}}\gamma}{(2\pi)^2} \int_{-\pi}^{\pi} \mathrm{d}\theta \int_0^{\infty} \mathrm{d}q \, \frac{q \, \mathrm{e}^{\mathrm{i}qr\cos\theta}}{k_E^2 - q^2}, \tag{3.7}$$

where A_{cell} is the area of the unit cell. The angular integral is the Bessel function [11]

$$J_0(qr) = \frac{1}{2\pi} \int_{-\pi}^{\pi} \mathrm{d}\theta \, \mathrm{e}^{\mathrm{i}qr\cos\theta}, \tag{3.8}$$

so that

$$g_0(\boldsymbol{r}) = \frac{A_{\text{cell}}\gamma}{2\pi} \int_0^{\infty} \mathrm{d}q \, \frac{q \, J_0(qr)}{k_E^2 - q^2}. \tag{3.9}$$

For large z, the Bessel function $J_0(z)$ has the asymptotic form $J_0(z) \sim \sqrt{2/(\pi z)}\cos\left(z - \frac{\pi}{4}\right)$ [11], so the integrand in Eq. (3.9) decays as $\sim q^{-3/2}$ for $q \to \infty$. This ensures convergence of the integral, considering the limit stated in Eq. (3.4).

3.3 Contour deformation and residue

To solve this integral, we split the Bessel function into a linear combination of Hankel functions, $J_0 = \frac{1}{2}(H_0^{(1)} + H_0^{(2)})$. Additionally, we use the continuation $H_0^{(2)}(\mathrm{e}^{-\mathrm{i}\pi}qr) = -H_0^{(1)}(qr)$ to fold the $H_0^{(2)}$ piece onto the negative axis [11]:

$$\begin{aligned} g_0(\boldsymbol{r}) &= \frac{A_{\text{cell}}\gamma}{4\pi} \int_0^{\infty} \mathrm{d}q \, \frac{q\left(H_0^{(1)}(qr) + H_0^{(2)}(qr)\right)}{k_E^2 - q^2} \\ &= \frac{A_{\text{cell}}\gamma}{4\pi} \left(\int_0^{\infty} \mathrm{d}q \, \frac{q \, H_0^{(1)}(qr)}{k_E^2 - q^2} + \int_0^{-\infty} (-\mathrm{d}q)(-q) \, \frac{H_0^{(2)}(\mathrm{e}^{\mathrm{i}\pi}qr)}{k_E^2 - q^2} \right) \\ &= \frac{A_{\text{cell}}\gamma}{4\pi} \int_{-\infty}^{\infty} \mathrm{d}q \, \frac{q \, H_0^{(1)}(qr)}{k_E^2 - q^2}. \end{aligned} \tag{3.10}$$

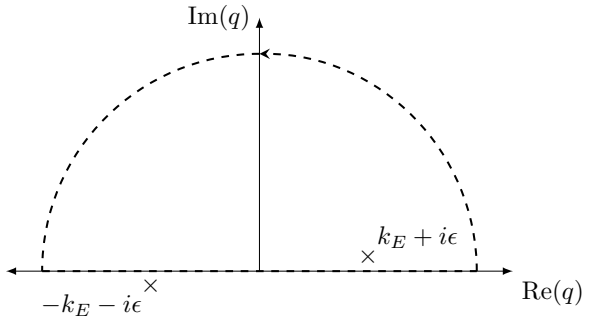


Figure 3.1: Integration contour for the q integral in Eq. (3.10). The integrand has poles at $q = \pm k_E$, which are shifted into the complex plane by $\pm i\epsilon$. The contour is closed in the upper half plane to pick up the outgoing solution.

For large z, $H_0^{(1)}(z) \sim \sqrt{2/(\pi z)}\, e^{i(z-\pi/4)}$ [11] decays in the upper half plane. The contour can be closed by a large semicircle as sketched in Fig. 3.1. Again considering the limit in Eq. (3.4), the poles at $q = \pm k_E$ are shifted into the complex plane by $\pm i\varepsilon$. For $k_E > 0$, the pole at $q > 0$ is the one enclosed. This is exactly the outgoing solution:

$$\begin{aligned} g_0(\boldsymbol{r}) &= \frac{A_{\text{cell}}\gamma}{4\pi}\, 2\pi\mathrm{i} \lim_{\varepsilon\to 0} \operatorname{Res}_{q=k_E+\mathrm{i}\varepsilon} \frac{q\, H_0^{(1)}(qr)}{(k_E+\mathrm{i}\varepsilon-q)(k_E+\mathrm{i}\varepsilon+q)} \\ &= -\frac{\mathrm{i}A_{\text{cell}}\gamma}{4}\, H_0^{(1)}(k_E r) = -\frac{\mathrm{i}A_{\text{cell}}}{4} v^{-2} H_0^{(1)}(k_E r). \end{aligned} \tag{3.11}$$

With this, we have a solution for g_0 of Eq. (3.5) and can now construct the Green's function.

3.4 The matrix Green's function

We now reinstate the numerator of Eq. (3.5) with $E = vk_E$ and $\mathcal{H}_0$ in position space ($q_x \to -\mathrm{i}\partial_x$, $q_y \to -\mathrm{i}\partial_y$). Using the identity $\partial_x \pm i\partial_y = e^{\pm i\theta}(\partial_r \pm i/r\, \partial_\theta)$ with $\theta = \arg(\boldsymbol{r})$, we calculate

$$\begin{aligned} G_0^\tau(\boldsymbol{r}; k_E) &= \left(E + \mathcal{H}_0^\tau(\boldsymbol{r})\right) g_0(\boldsymbol{r}) \\ &= \left[vk_E\, \mathbb{1}_2 + v \begin{pmatrix} 0 & -\tau\mathrm{i}\partial_y + \partial_x \\ -\tau\mathrm{i}\partial_y - \partial_x & 0 \end{pmatrix}\right] \left(-A_{\text{cell}} \frac{\mathrm{i}}{4} v^{-2} H_0^{(1)}(k_E r)\right) \\ &= -\frac{\mathrm{i}k_E A_{\text{cell}}}{4} v^{-1} \begin{pmatrix} H_0^{(1)}(k_E r) & -\mathrm{e}^{-\tau\mathrm{i}\theta} H_1^{(1)}(k_E r) \\ \mathrm{e}^{\tau\mathrm{i}\theta} H_1^{(1)}(k_E r) & H_0^{(1)}(k_E r) \end{pmatrix}, \end{aligned} \tag{3.12}$$

where the last step uses $\partial_r H_0^{(1)}(k_E r) = -k_E H_1^{(1)}(k_E r)$ [11].

The entries of the Green's function are labelled by pairs of lattice sites, so Eq. (3.12) is to be understood as a continuum expression that is evaluated only at the separations between the sites. No continuum approximation for the positions is involved, including the identity $q_x \to -i\partial_x$. Under the Fourier integral Eq. (3.7), this is an exact identity.

For a sufficiently large system, the $\boldsymbol{k}$ space is continuous, and the integral in Eq. (3.7) is valid. This is where the continuum approximation enters. Not limiting this integral to the first Brillouin zone is an approximation. However, this is expected to be valid in the large-r limit, as there the largest contribution to the integral comes from the region near $q = 0$.

With this in mind, the approximate Green's function will be compared to the numerical Green's function in Chapter 4, and the validity of the approximation will be discussed.

Chapter 4

Numerical evaluation of the lattice Green's function

In this chapter, the Green's function is evaluated numerically and compared to the Dirac approximation. Additionally, due to the $r = 0$ divergence of the approximation, the exact analytical solution of the Green's function is derived to compare it to the numerical integration over the Brillouin zone.

4.1 Integral representation of the Green's function

For the numerical calculation of the Green's function, we will use the definition Eq. (3.3) to derive an integral expression. As stated above, the Green operator is defined as [10]

$$G_0(z) = (z - \mathcal{H}_0)^{-1}. \tag{4.1}$$

Inverting this expression in the eigenbasis of $\mathcal{H}_0$ and performing a Fourier transform gives the integral representation of the Green's function in real space

$$G_0(\boldsymbol{r}; z) = \frac{A_{\text{cell}}}{(2\pi)^2} \int_{\text{BZ}} \mathrm{d}^2k \frac{1}{z^2 - t^2|f(\boldsymbol{k})|^2} \begin{pmatrix} z & -tf(\boldsymbol{k}) \\ -tf^*(\boldsymbol{k}) & z \end{pmatrix} e^{i\boldsymbol{k}\cdot\boldsymbol{r}}. \tag{4.2}$$

This is evaluated numerically using a rectangle rule with $N \times N$ points in the Brillouin zone. Writing $\boldsymbol{k} = u_1\boldsymbol{b}_1 + u_2\boldsymbol{b}_2$ with $u_i \in \{0, 1/N, \ldots, (N-1)/N\}$ makes the rectangle rule exactly periodic. Thus, no endpoint correction is needed. The integral is evaluated for $z = E + i\varepsilon$. It is worth noting that decreasing ε increases the resolution of the pole ridge, but also either increases the numerical error or requires more computational time. A compromise balancing those effects has to be made.

This numerical evaluation can now be used to compare the Dirac approximation of the Green's function to the exact lattice result. The comparison is done in Section 4.3. First, however, the exact analytical solution of the Green's function at zero distance is derived in Section 4.2.

4.2 The analytical zero solution

The zero solution, namely $G_0(0;z)$, is necessary not only to compare the numerics to the analytical results but also for the self-consistency condition in Section 5.1. However, it is divergent in our Dirac approximation. The exact analytical solution is needed to guarantee a finite value.

For this, the integral in Eq. (4.2) can be rearranged into a form analytically solved by Horiguchi [12]. This is done in Appendix A. The integral is reduced to a triangular lattice integral, which can be expressed in terms of elliptic integrals. The relation between G^{AA} at zero distance in our setup and in Horiguchi's setup is

$$G_0^{AA} = \frac{1}{2t} G_{\mathrm{H}}^{AA}\left(t_{\mathrm{H}} = \frac{w}{2}\right), \tag{4.3}$$

with $w = z/t$. Using this relation, we find the exact analytical value of G_0^{AA}. We write

$$G_0^{AA}(0;z) = \frac{1}{2t} G_{\mathrm{H}}^{AA}(0,0) = \frac{1}{2t} 2t_H G_t(\frac{1}{2}(4t_H^2 - 3); 0, 0) \tag{4.4}$$

and

$$G_t(t;0,0) = \frac{1}{2\pi} g K(k^2), \tag{4.5}$$

where

$$\begin{aligned} g &= \frac{8}{[(2t+3)^{1/2}-1]^{\frac{3}{2}}[(2t+3)^{1/2}+3]^{\frac{1}{2}}}, \\ k &= \frac{4(2t+3)^{1/4}}{[(2t+3)^{1/2}-1]^{\frac{3}{2}}[(2t+3)^{1/2}+3]^{\frac{1}{2}}} \quad \text{and} \\ K(k^2) &= \int_0^{\pi/2} \frac{\mathrm{d}\phi}{\sqrt{1-k^2\sin^2\phi}}. \end{aligned}$$

With $4t_H^2 = w^2$, we now have the expression

$$\begin{aligned} G_0^{AA}(0;z) &= \frac{1}{2t} w G_t(\frac{1}{2}(w^2-3); 0, 0) \\ &= \frac{1}{4t}\frac{w}{\pi} g K(k^2), \end{aligned} \tag{4.6}$$

with $g = 8/([w-1]^{3/2}[w+3]^{1/2})$ and $k = 4w^{1/2}/([w-1]^{3/2}[w+3]^{1/2})$. This is the exact analytical value of $G_0^{AA}(0)$.

For $w > 3$, i.e. outside the band, g and k^2 are real and the expression can be evaluated directly. Inside the band, the retarded Green's function follows by analytic continuation from $w > 3$ through the upper half plane, $z = E + i0$. For $0 < E < t$, i.e. $0 < w < 1$, this gives $(w-1)^{3/2} = -i(1-w)^{3/2}$ in g, and the elliptic integral has to be taken on the branch

$$K(k^2) \;\to\; K(k^2) + 2i\,K(1-k^2), \tag{4.7}$$

where $k^2 < 0$ and $1 - k^2 > 1$ lies just above the branch cut of K. Evaluating $K(k^2)$ on its principal branch instead gives the wrong sign of $\mathrm{Im}\, G_0^{AA}$ and misses the logarithmic term.

As stated before, this result can also be used to verify the numerical integration over the Brillouin zone. At $r = 0$, the numerics are compared against the exact analytical lattice result, so this is a pure quadrature test.

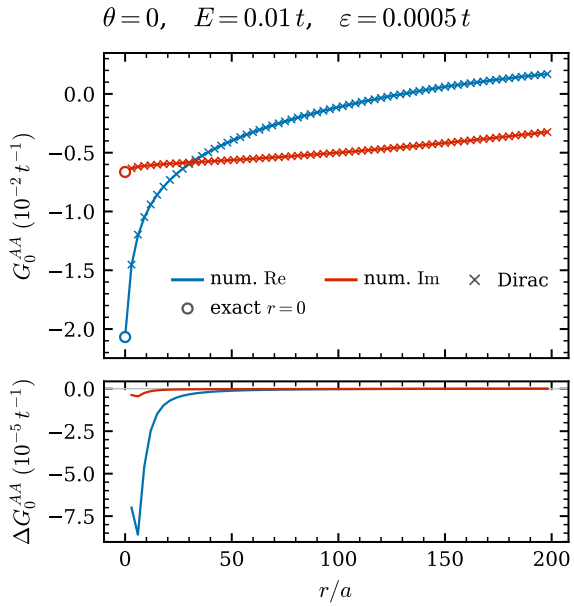


Figure 4.1: The figure shows the imaginary and real parts of the numerical result and of the Dirac approximation, as well as their difference, for different r in the AA component. At zero, the numerical result is compared to the exact solution, which is given by the relation to the Horiguchi result.

4.3 Numerical validation against the Dirac approximation

Using G_0 for each valley from Chapter 3, the total Green's function as a sum of the two valleys

$$G_0(\boldsymbol{r}; z) = e^{i\boldsymbol{K}\cdot\boldsymbol{r}} G_0^K(\boldsymbol{r}; z) + e^{i\boldsymbol{K}'\cdot\boldsymbol{r}} G_0^{K'}(\boldsymbol{r}; z) \tag{4.8}$$

is constructed. The numerical evaluation of the Brillouin zone integral is compared to the Dirac approximation in Fig. 4.1. Note that each component has to be evaluated at separations between sites of the corresponding sublattices. The diagonal components connect sites of the same sublattice, while the off-diagonal components include an additional shift by $\pm\boldsymbol{\delta}_1$. Additionally, the same positive ε in $z = E + i\varepsilon$ is used for both the numerical and the analytical result to ensure that the outgoing solution is selected.

The comparison shows that the Dirac approximation describes the Green's function well for large r but fails to describe the Green's function at small r. This confirms the expectations stated in Section 3.4. In Chapter 5, the cross section will be derived. This is a quantity defined in the far field. With the results of this chapter, the Dirac approximation is deemed suitable to describe its properties for low-energy scattering.

Additionally, we now construct the Green's function with the exact value at $r = 0$ and the far-field approximation for $r > 0$. This result will be used in Chapter 5 to solve the Lippmann-Schwinger equation for a single impurity.

Chapter 5

Solution of the Lippmann-Schwinger equation for a single impurity

In the previous chapters, we have derived results for the Dirac Green's function and compared them to the numerical solution. In this chapter, those results will be used to solve the Lippmann-Schwinger equation for a single impurity in the graphene lattice. From the scattered wave, the scattering amplitude and the cross section will be derived and discussed.

5.1 Lippmann-Schwinger equation and self-consistency condition

The single-site impurity is described by the potential $V(\boldsymbol{r}_i) = V_0 P(\boldsymbol{r}_0)$, where $P(\boldsymbol{r}_0)$ is a projection operator onto the $\boldsymbol{r}_0$ lattice site and V_0 is the strength of the potential. For a vacancy, there can be no state at $\boldsymbol{r}_0$ in the tight-binding model, so $V_0 \to \infty$ is the appropriate limit [5]. However, this model ignores the slight local distortion of the lattice, which is expected around a real vacancy [5].

Using the Lippmann-Schwinger equation in position representation Eq. (3.2), we find for a single impurity at $\boldsymbol{r}_0$

$$\begin{aligned} \psi(\boldsymbol{r}) &= \psi_{\text{in}}(\boldsymbol{r}) + G_0(\boldsymbol{r}-\boldsymbol{r}_0;E)V_0\psi^{\alpha}(\boldsymbol{r}_0) \\ &= \psi_{\text{in}}(\boldsymbol{r}) + \psi_{\text{sc}}(\boldsymbol{r}), \end{aligned} \tag{5.1}$$

where $\alpha \in \{A, B\}$ denotes the sublattice of $\boldsymbol{r}_0$.

We note that, for $E \ll |t|$, the Green's function $G_0(\boldsymbol{r}-\boldsymbol{r}_0;E)$ is approximated by

$$G_0(\boldsymbol{r}-\boldsymbol{r}_0;E) = e^{i\boldsymbol{K}\cdot(\boldsymbol{r}-\boldsymbol{r}_0)}G_0^{\boldsymbol{K}}(\boldsymbol{r}-\boldsymbol{r}_0;E) + e^{i\boldsymbol{K}'\cdot(\boldsymbol{r}-\boldsymbol{r}_0)}G_0^{\boldsymbol{K}'}(\boldsymbol{r}-\boldsymbol{r}_0;E), \tag{5.2}$$

with

$$G_0^{\boldsymbol{K}^\tau}(\boldsymbol{r}-\boldsymbol{r}_0;E) = -A_{\text{cell}}\frac{ik_E}{4v}\begin{pmatrix} H_0^{(1)}(k_E|\boldsymbol{r}-\boldsymbol{r}_0|) & -e^{-i\tau\theta}H_1^{(1)}(k_E|\boldsymbol{r}-\boldsymbol{r}_0|) \\ e^{i\tau\theta}H_1^{(1)}(k_E|\boldsymbol{r}-\boldsymbol{r}_0|) & H_0^{(1)}(k_E|\boldsymbol{r}-\boldsymbol{r}_0|) \end{pmatrix}. \tag{5.3}$$

This yields the self-consistency condition

$$\psi^{\alpha}(\boldsymbol{r}_0) = \frac{\psi_{\text{in}}^{\alpha}(\boldsymbol{r}_0)}{1 - V_0 G_0^{\alpha\alpha}(0;E)}, \tag{5.4}$$

where $G_0^{\alpha\alpha}(0;E)$ is finite and is derived in Chapter 4.

5.2 Incoming plane wave

For the self-consistency condition, we need to consider the incoming wave. We are interested in the scattering of a plane wave. The incoming wave is modelled as a plane wave with momentum $\boldsymbol{k}$ close to either the $\boldsymbol{K}$ or $\boldsymbol{K'}$ point. We can write the incoming wave as

$$\psi_{\text{in}}^{\tau}(\boldsymbol{r}) = e^{i(\boldsymbol{K}^{\tau}+\boldsymbol{q})\cdot\boldsymbol{r}}\chi_{\boldsymbol{k}}^{\tau}(\varphi), \tag{5.5}$$

with $\chi_{\boldsymbol{k}}^{\tau}(\varphi)$ being the eigenvector of the unperturbed Dirac Hamiltonian Eq. (2.7) for positive energy, where we used the approximation Eq. (2.10).

The phase factor $e^{i(\boldsymbol{K}^{\tau}+\boldsymbol{q})\cdot\boldsymbol{r}_0}$ only contributes an overall phase to the scattered wave and does not affect the scattering amplitude or the cross section. One can therefore set $\boldsymbol{r}_0 = 0$, i.e. place the origin on the A- or B-sublattice impurity, without loss of generality. In the case of a B-sublattice impurity, the self-consistency condition also contains the phase factor $-ie^{i\tau\varphi}$, which similarly does not affect the scattering amplitude and cross section.

5.3 Scattered wave and scattering amplitude

We now consider the scattered wave. We model the incoming wave as a plane wave and choose $\boldsymbol{r}_0 = 0$ at an A-site impurity. Using Eq. (5.1) and the self-consistency condition, we find

$$\psi_{\text{sc}}(\boldsymbol{r}) = -\frac{ik_E V_0 R A_{\text{cell}}}{4v}\left[e^{i\boldsymbol{K}\cdot\boldsymbol{r}}\begin{pmatrix} H_0^{(1)}(k_E r) \\ e^{i\theta}H_1^{(1)}(k_E r)\end{pmatrix} + e^{i\boldsymbol{K'}\cdot\boldsymbol{r}}\begin{pmatrix} H_0^{(1)}(k_E r) \\ e^{-i\theta}H_1^{(1)}(k_E r)\end{pmatrix}\right], \tag{5.6}$$

where $R = 1/(\sqrt{2}(1-V_0 G_0^{AA}(0;E)))$. It is worth noting [redacted] as previously, the upper component corresponds to A sites and the lower one to B sites.

In the limit $V_0 \to \infty$ of a vacancy, the prefactor $V_0 R$ converges to a finite value. The scattering amplitude is therefore finite, and the scattering cross section is nonzero.

The scattering amplitude is a far-field quantity, so using the asymptotic form of the Hankel functions $H_\nu^{(1)}(z) \sim \sqrt{2/(\pi z)}e^{i(z-\nu\pi/2-\pi/4)}$ [11], we find for $k_E r \gg 1$:

$$\begin{aligned}
\psi_{\text{sc}}(\boldsymbol{r}) &= -\frac{ik_E V_0 R A_{\text{cell}}}{4v}\sqrt{\frac{2}{\pi k_E r}}e^{i(k_E r-\pi/4)}\left[e^{i\boldsymbol{K}\cdot\boldsymbol{r}}\begin{pmatrix}1\\ -ie^{i\theta}\end{pmatrix} + e^{i\boldsymbol{K'}\cdot\boldsymbol{r}}\begin{pmatrix}1\\ -ie^{-i\theta}\end{pmatrix}\right] \\
&= \frac{e^{ik_E r}}{\sqrt{r}}\left[f^{+}(\theta)e^{i\boldsymbol{K}\cdot\boldsymbol{r}}\frac{1}{\sqrt{2}}\begin{pmatrix}1\\ -ie^{i\theta}\end{pmatrix} + f^{-}(\theta)e^{i\boldsymbol{K'}\cdot\boldsymbol{r}}\frac{1}{\sqrt{2}}\begin{pmatrix}1\\ -ie^{-i\theta}\end{pmatrix}\right] \\
&= \frac{e^{ik_E r}}{\sqrt{r}}\left[f^{+}(\theta)e^{i\boldsymbol{K}\cdot\boldsymbol{r}}\chi^{+}(\theta) + f^{-}(\theta)e^{i\boldsymbol{K'}\cdot\boldsymbol{r}}\chi^{-}(\theta)\right],
\end{aligned} \tag{5.7}$$

with the scattering amplitudes

$$f^{\tau}(\theta) = -\frac{ik_E V_0 R A_{\text{cell}}}{4v}\sqrt{\frac{2}{\pi k_E}}e^{-i\pi/4}\sqrt{2} = -\frac{iV_0 R A_{\text{cell}}}{2v}\sqrt{\frac{k_E}{\pi}}e^{-i\pi/4}. \tag{5.8}$$

This result will now be used to find the scattering cross section in the next section.

5.4 Scattering cross section

To determine the scattering cross section, we need to calculate the current density

$$\boldsymbol{j} = \frac{1}{2}\left(\psi^\dagger \hat{v}\psi + (\psi^\dagger \hat{v}\psi)^\dagger\right) = \psi^\dagger \hat{v}\psi, \tag{5.9}$$

with $\hat{v} = \partial\mathcal{H}/(\partial \boldsymbol{p})$. Around $\boldsymbol{K}^\tau$, this yields

$$\hat{v}^\tau = \frac{v}{\hbar}\begin{pmatrix} -\sigma_y \\ \tau\sigma_x \end{pmatrix}. \tag{5.10}$$

We can now calculate the current density of the scattered wave and the incoming wave. We find

$$\boldsymbol{j}^\tau_{\text{in}} = \frac{v}{\hbar}\begin{pmatrix}\cos(\varphi)\\ \sin(\varphi)\end{pmatrix} \quad \text{and} \quad \boldsymbol{j}^\tau_{\text{sc}} = \frac{v|f^\tau(\theta)|^2}{\hbar r}\begin{pmatrix}\cos(\theta)\\ \sin(\theta)\end{pmatrix}. \tag{5.11}$$

Looking at the radial component of the scattered current density and the absolute value of the incoming current density, we can now calculate

$$j^\tau_{\text{sc},r} = \boldsymbol{j}^\tau \cdot \hat{\boldsymbol{r}} = \frac{v|f^\tau(\theta)|^2}{\hbar r}, \quad |\boldsymbol{j}^\tau_{\text{in}}| = \frac{v}{\hbar}. \tag{5.12}$$

Using the definition of the 2D differential scattering cross section, we find

$$\mathrm{d}\sigma^\tau = \frac{\text{flux scattered into } \mathrm{d}\theta}{\text{incident flux}} = \frac{r j^\tau_{\text{sc},r}}{|\boldsymbol{j}^\tau_{\text{in}}|}\mathrm{d}\theta = |f^\tau(\theta)|^2 \mathrm{d}\theta. \tag{5.13}$$

For the cross section per valley, we integrate over the full angle $0 \le \theta < 2\pi$

$$\sigma^\tau = \int_0^{2\pi} \frac{\mathrm{d}\sigma^\tau}{\mathrm{d}\theta}\mathrm{d}\theta = 2\pi|f^\tau(\theta)|^2, \tag{5.14}$$

and for the total cross section

$$\sigma = \sum_\tau \sigma^\tau = 4\pi|f^\tau(\theta)|^2 = \frac{V_0^2|R|^2 k_E A_{\text{cell}}^2}{v^2}. \tag{5.15}$$

The scattering amplitude $f^\tau(\theta)$ is completely independent of θ and τ and depends on the angle φ of the incoming wave only through a phase factor. As a result, the cross section is isotropic, independent of the valley index τ and the same for all angles of incoming waves. The valleys are therefore completely mixed. This is expected, as the delta potential is constant in momentum space.

A known result for the scattering cross section of a single impurity in graphene is given by Basko [6]. However, in that work, the low-energy expansion of $G_0^{\alpha\alpha}(0;E)$ contains a parameter r_0 (no relation to the $\boldsymbol{r}_0$ we used before), whose value was determined by numerical integration over the Brillouin zone to be $r_0 e^\gamma = a$. In Appendix B, we show that, using the exact value of $G_0^{\alpha\alpha}(0;E)$, this result follows analytically for low energies.

5.5 Optical theorem

As a consistency check of the scattering amplitude and the cross section, we verify the optical theorem [13]. For this, we use current conservation. It states that, for elastic scattering, the net flux of $\psi = \psi_{\text{in}}^{\tau} + \psi_{\text{sc}}$ through a large circle of radius r around the impurity has to vanish. Put simply, any wave that enters the circle must also leave it. We consider the A-site impurity of the previous sections.

The radial current consists of three parts. The incoming plane wave alone gives no net flux through the circle. The scattered wave alone gives the flux $v\sigma/\hbar$, with the total cross section σ summed over both final valleys. The third part is the interference of ψ_{in}^{τ} and ψ_{sc}. Here, only the part of ψ_{sc} in the incoming valley τ contributes, as the terms connecting different valleys carry the factor $e^{\pm i(\boldsymbol{K}-\boldsymbol{K}')\cdot\boldsymbol{r}}$, which oscillates on the lattice scale and averages out along the circle.

With current conservation, the scattered wave and thus the cross section is determined by the interference term. With this, we derive the optical theorem, stating that the total cross section is proportional to the imaginary part of the scattering amplitude in the forward direction.

To evaluate the interference term, we note that the spinor of the scattered wave is an eigenvector of the radial velocity,

$$\hat{\boldsymbol{r}} \cdot \hat{v}^{\tau}\, \chi^{\tau}(\theta) = \frac{v}{\hbar}\, \chi^{\tau}(\theta), \qquad \chi^{\tau\dagger}(\varphi)\, \chi^{\tau}(\theta) = \frac{1}{2}\left(1 + e^{i\tau(\theta-\varphi)}\right), \tag{5.16}$$

where $\hat{\boldsymbol{r}} = (\cos\theta, \sin\theta)$ and the incoming spinor $\chi_{\boldsymbol{k}}^{\tau}(\varphi)$ has the same form as $\chi^{\tau}(\theta)$ with $\theta \to \varphi$. With $\boldsymbol{q}\cdot\boldsymbol{r} = k_E r\cos(\theta-\varphi)$, the interference current is

$$j_{\text{int},r}^{\tau} = 2\,\text{Re}\left[\psi_{\text{in}}^{\tau\dagger}\,(\hat{\boldsymbol{r}}\cdot\hat{v}^{\tau})\,\psi_{\text{sc}}\right] = \frac{v}{\hbar}\,\text{Re}\left[\left(1 + e^{i\tau(\theta-\varphi)}\right) f^{\tau}(\theta)\,\frac{e^{ik_E r(1-\cos(\theta-\varphi))}}{\sqrt{r}}\right]. \tag{5.17}$$

For $k_E r \gg 1$, the phase oscillates rapidly, except at the stationary points $\theta = \varphi$ and $\theta = \varphi + \pi$. In the backward direction, the spinor overlap $1 + e^{i\tau\pi}$ vanishes, so only the forward direction contributes. Expanding $1 - \cos(\theta-\varphi) \sim (\theta-\varphi)^2/2$ and using $\int \mathrm{d}\alpha\, e^{ik_E r\alpha^2/2} = \sqrt{2\pi/(k_E r)}\, e^{i\pi/4}$ gives

$$\int_0^{2\pi} r\, j_{\text{int},r}^{\tau}\,\mathrm{d}\theta = \frac{2v}{\hbar}\sqrt{\frac{2\pi}{k_E}}\,\text{Re}\left[e^{i\pi/4} f^{\tau}(\varphi)\right]. \tag{5.18}$$

The flux balance $v\sigma/\hbar + \int r\, j_{\text{int},r}^{\tau}\,\mathrm{d}\theta = 0$ then yields the optical theorem in two dimensions,

$$\sigma = \sqrt{\frac{8\pi}{k_E}}\,\text{Im}\left[e^{-i\pi/4} f^{\tau}(\varphi)\right]. \tag{5.19}$$

We now insert our result for f^{τ}. With $e^{-i\pi/4} f^{\tau} = -V_0 R A_{\text{cell}}\sqrt{k_E/\pi}/(2v)$ and

$$\text{Im}\,(V_0 R) = \frac{V_0^2\,\text{Im}\,G_0^{AA}(0;E)}{\sqrt{2}\,|1 - V_0 G_0^{AA}(0;E)|^2} = \sqrt{2}\,V_0^2 |R|^2\,\text{Im}\,G_0^{AA}(0;E), \tag{5.20}$$

the right-hand side of Eq. (5.19) becomes

$$\sqrt{\frac{8\pi}{k_E}}\,\text{Im}\left[e^{-i\pi/4} f^{\tau}\right] = -\frac{\sqrt{2}A_{\text{cell}}}{v}\,\text{Im}\,(V_0 R) = -\frac{2A_{\text{cell}} V_0^2 |R|^2}{v}\,\text{Im}\,G_0^{AA}(0;E). \tag{5.21}$$

Comparing with $\sigma = V_0^2|R|^2 k_E A_{\text{cell}}^2/v^2$, the optical theorem holds for all V_0 if and only if

$$\operatorname{Im} G_0^{AA}(0;E) = -\frac{A_{\text{cell}} k_E}{2v} = -\frac{A_{\text{cell}} E}{2v^2}. \tag{5.22}$$

This condition can be checked directly using the low-energy result for $G_0^{AA}(0;E)$ derived in Appendix B. We find

$$\operatorname{Im} G_0^{AA}(0;E) = -\frac{A_{\text{cell}} E}{2v^2}, \tag{5.23}$$

which is exactly Eq. (5.22). The imaginary part of $G_0^{AA}(0;E)$ is $-\pi$ times the local density of states per spin on a lattice site.

The optical theorem is therefore fulfilled for any impurity strength V_0, independently of $\operatorname{Re} G_0^{AA}(0;E)$. This is a non-trivial check of the scattering amplitude: it tests the normalisation R, the factors A_{cell}, the far-field form of the Hankel functions and the use of the exact lattice value at $\boldsymbol{r} = 0$ at the same time.

5.6 Conductivity for a density of impurities

Using the scattering cross section, we can now determine some transport properties of a graphene sample with a density of impurities. We consider a density of impurities n and determine the conductivity σ_{el} of the sample.

Using $n\sigma_{tr} l = 1$, where σ_{tr} is the transport cross section and l is the mean free path, we can determine the conductivity for a density of impurities. We use the relation $\sigma_{\text{el}} = e^2\rho(E_F)D$ [4] with $D = v^2/(2\hbar^2)\tau_{tr}$, where $\tau_{tr} = l/(v/\hbar)$ is the transport time and $\rho(E_F)$ is the density of states at the Fermi energy. We find

$$\sigma_{\text{el}} = \frac{e^2 v}{2\hbar n \sigma_{tr}} \rho(E_F). \tag{5.24}$$

Note that the transport cross section per valley is given by

$$\sigma_{tr}^{\tau} = \int_0^{2\pi} |f^{\tau}(\theta)|^2 (1 - \cos(\theta)) d\theta, \tag{5.25}$$

which in our case yields exactly $\sigma_{tr} = \sigma$ for the total transport cross section. The density of states of graphene per unit cell, including spin and valley degeneracy, is the well-known result $2A_{\text{cell}}|E|/(\pi v^2)$ [2]. Per unit area, this gives $\rho(E_F) = 2|E_F|/(\pi v^2)$ with $E_F = v k_F$. We can therefore write the conductivity as

$$\sigma_{\text{el}} = \frac{e^2}{\hbar}\frac{k_F}{\pi n \sigma} = \frac{e^2}{\hbar\pi}\frac{v^2}{n A_{\text{cell}}^2 V_0^2 |R|^2} \overset{V_0 \text{ large}}{=} \frac{2e^2}{\hbar\pi}\frac{v^2 |G_0^{AA}(0;E_F)|^2}{n A_{\text{cell}}^2}, \tag{5.26}$$

where we used for large V_0

$$\lim_{V_0 \to \infty} V_0^2 |R|^2 = \frac{1}{2|G_0^{AA}(0;E_F)|^2}. \tag{5.27}$$

5.7 Conductivity at low energies

In Section 5.6, we expressed the conductivity in terms of the exact Green's function at zero distance. For low energies, this result can be written in a more transparent form. For this, we use the low-energy expansion of $G_0^{AA}(0; E_F)$ derived in Appendix B,

$$G_0^{AA}(0; E_F) \sim -\frac{A_{\text{cell}} E_F}{\pi v^2} \left(\ln\left(\frac{2v}{aE_F}\right) + \frac{i\pi}{2} \right), \tag{5.28}$$

which is valid for $E_F \ll t$. Its imaginary part agrees with Eq. (5.22). Inserting this into Eq. (5.26) gives

$$\sigma_{\text{el}} = \frac{2e^2}{\hbar\pi} \frac{E_F^2}{\pi^2 v^2 n} \left[\ln^2\left(\frac{2}{k_F a}\right) + \frac{\pi^2}{4} \right]. \tag{5.29}$$

The carrier density follows from the density of states. Including spin and valley degeneracy, we find

$$n_e = \int_0^{E_F} \rho(E)\, \mathrm{d}E = \frac{E_F^2}{\pi v^2} = \frac{k_F^2}{\pi}. \tag{5.30}$$

With $\hbar = h/(2\pi)$, we obtain

$$\sigma_{\text{el}} = \frac{4e^2}{\pi h} \frac{n_e}{n} \left[\ln^2\left(\frac{2}{k_F a}\right) + \frac{\pi^2}{4} \right]. \tag{5.31}$$

The conductivity is determined by the ratio of carrier density to impurity density only, up to the logarithm, and contains no free parameter. It grows approximately linearly with n_e with a logarithmic correction. As the logarithm dominates for $k_F a \ll 1$, the term $\pi^2/4$ is only a small correction in the low-energy regime.

It is worth noting that vacancies create so-called midgap states. These are localised states with an energy at or close to the Dirac point [14, 15]. The $\ln^2$ dependence of the conductivity is characteristic for scattering off vacancies [15] and other strong scatterers [16].

The result derived in Section 5.6 relies on the semiclassical Boltzmann picture. There, the electrons perform a classical diffusive random walk and scatter independently off the different impurities [4]. This is only justified if an electron travels over many wavelengths between two scattering events, i.e. if $k_F l \gg 1$. Using $l = 1/(n\sigma)$ in Eq. (5.26), we find

$$k_F l = \frac{\pi\hbar}{e^2}\, \sigma_{\text{el}} = \frac{h}{2e^2}\, \sigma_{\text{el}}. \tag{5.32}$$

Thus, Eq. (5.31) is only valid as long as $\sigma_{\text{el}} \gg e^2/h$. Close to the Dirac point, where $n_e \to 0$, this condition fails and the semiclassical description breaks down.

In the next section, we compare Eq. (5.31) to other theoretical results and to a measurement.

5.8 Comparison with other results

In this section, we compare the conductivity Eq. (5.31) to results from the literature. First, we consider two other theoretical descriptions of strong impurities. Afterwards, we compare it to a measurement on ion-irradiated graphene.

The lattice model of Wehling et al. [17] describes adsorbates such as H, CH_3 or C_2H_5 by an additional orbital with energy ϵ_d, which is coupled by a hopping V to a single carbon atom at $\boldsymbol{r}_0$. For an eigenstate with energy E, the amplitude ψ_d on the additional orbital fulfils

$$E\,\psi_d = \epsilon_d\,\psi_d + V\psi^\alpha(\boldsymbol{r}_0) \qquad \Longrightarrow \qquad \psi_d = \frac{V}{E-\epsilon_d}\,\psi^\alpha(\boldsymbol{r}_0). \tag{5.33}$$

In the equation for $\psi^\alpha(\boldsymbol{r}_0)$, the orbital enters through the term $V\psi_d$. Inserting ψ_d gives

$$V\psi_d = \frac{V^2}{E-\epsilon_d}\,\psi^\alpha(\boldsymbol{r}_0), \tag{5.34}$$

which acts like an energy-dependent potential on the carbon site. This is exactly the single-site impurity of this chapter with

$$V_0 \to \frac{V^2}{E-\epsilon_d}. \tag{5.35}$$

From density functional calculations, Wehling et al. find $|V| \gtrsim 2t$ and $|\epsilon_d| \lesssim 0.1\,t$ for these adsorbates. Close to the Dirac point, this gives $|V_0| \gtrsim 40\,t$, so the limit $V_0 \to \infty$ also describes such adsorbates approximately. In the limit $V \to \infty$, which corresponds to $V_0 \to \infty$, their Boltzmann result is

$$\sigma_\mathrm{el} \sim \frac{4e^2}{\pi h}\,\frac{n_e}{n}\,\ln^2\left|\frac{E_F}{D}\right|, \qquad D = \sqrt{\sqrt{3}\pi}\,t \approx 2.33\,t. \tag{5.36}$$

It has the same prefactor as Eq. (5.31). The imaginary parts of the local Green's functions agree as well. The difference lies in the cutoff of the logarithm. Wehling et al. approximate the density of states per spin and carbon atom by the linear function $|E|/D^2$ up to the cutoff D. With the value of D above, its slope agrees with the Dirac cone and it contains exactly one state per carbon atom and spin. This corresponds to $\ln^2(k_F R)$ with $R = v/D \approx 0.64\,a$. In our result, the cutoff follows from the exact lattice Green's function at zero distance, which gives $R = a/2$.

A second description is the continuum model of Stauber et al. [15]. There, a vacancy of radius R_0 enters through the s-wave phase shift $\delta_k = -\pi/(2\ln(kR_0))$. Chen et al. quote the resulting conductivity as [18]

$$\sigma_\mathrm{el} = \frac{2e^2}{\pi h}\,\frac{n_e}{n}\,\ln^2(k_F R_0), \tag{5.37}$$

which is a factor of two smaller than both lattice results.

Finally, we compare our result to the measurement of Chen et al. [18]. They irradiated graphene on SiO_2 with 500 eV Ne^+ and He^+ ions in ultra-high vacuum at low temperature and measured its conductivity. Referring to earlier studies of ion-irradiated graphite, they state that ion irradiation at these energies produces one atomic-scale defect per incident ion. According to them, this defect is most likely a carbon vacancy with a trapped rare-gas molecule. With one defect per ion, the defect density n equals the ion dose.

To analyse their data, Chen et al. fit the measured conductivity with a constant mobility $\mu = \sigma_\mathrm{el}/(en_e)$ and a density-independent resistivity. They find that μ^{-1} increases linearly with the dose,

$$\mu^{-1} = 7.9 \times 10^{-16}\,\mathrm{V\,s} \times n \;\;(\mathrm{Ne}^+), \qquad \mu^{-1} = 9.3 \times 10^{-16}\,\mathrm{V\,s} \times n \;\;(\mathrm{He}^+). \tag{5.38}$$

They attribute this increase to uncharged lattice defects. One of their arguments is that charged impurities would require about four added charges per incident ion. The shift of the gate voltage of minimum conductivity, however, indicates only about 1/5 of a net charge per ion.

Assuming Eq. (5.37) at $n_e = 2 \times 10^{12}\,\mathrm{cm}^{-2}$, Chen et al. obtain a defect radius $R_0 = 2.3\,\text{Å}$ for Ne^+ and $R_0 = 2.9\,\text{Å}$ for He^+. They describe this as a reasonable value for single-carbon vacancies generated by ion knock-off. With this radius, the predicted conductivity is similar in magnitude to the measured one. However, it has a stronger sublinearity, i.e. it bends more strongly away from a linear dependence on n_e. They state that they do not understand this discrepancy. According to them, it may be related to carrier density inhomogeneity or to the addition of a small amount of deep charged impurities. They further report that the mobility partially recovers after heating to 485 K between runs, possibly due to annealing or passivation of the defects.

We now compare these slopes to our result. At the same carrier density $n_e = 2 \times 10^{12}\,\mathrm{cm}^{-2}$, we have $k_F a = 0.036$, and Eq. (5.31) gives

$$\mu^{-1} = \frac{\pi h}{4e}\left[\ln^2\left(\frac{2}{k_F a}\right) + \frac{\pi^2}{4}\right]^{-1} n = 1.7 \times 10^{-16}\,\mathrm{V\,s} \times n. \tag{5.39}$$

The slopes measured by Chen et al. are larger than this value by a factor of 4.5 for Ne^+ and 5.3 for He^+.

It seems that the derived theoretical prediction misses some physical effects. However, investigating this exceeds the scope of this work, so we will not pursue it further. In the next chapter, we consider an impurity in a graphene quantum dot.

Chapter 6

Quantum dot formalism and eigenstates

Until now, we have only considered a plain graphene sheet. In this chapter, we will consider a quantum dot on this sheet. The quantum dot breaks the sublattice symmetry in some area, which can be described by a mass term in the Hamiltonian. We will derive the eigenstates of this modified Hamiltonian and discuss the effect of an impurity with perturbation theory.

6.1 The modified Hamiltonian

From the previous chapters, we have seen that the Hamiltonian of graphene around the Dirac point with valley index τ can be written as

$$\mathcal{H}_0^\tau = v\left(\tau q_y \sigma_x - q_x \sigma_y\right), \tag{6.1}$$

where v is defined as in Chapter 2, and σ_x, σ_y are the Pauli matrices. When we consider a quantum dot, an additional energy term is added. We write

$$\mathcal{H}^\tau = \mathcal{H}_0^\tau + \Delta(r)\sigma_z, \tag{6.2}$$

where $\Delta(r)$ is a function that describes the mass term of the quantum dot. The term $\Delta(\boldsymbol{r})\sigma_z$ represents the energy gap induced by the confinement, which can vary with position r and defines the geometry of the quantum dot. In our case, we will consider a circular quantum dot, which can be described by a step function in the mass term. In Refs. [19, 20], the mass term acts as a hard wall, i.e. it is infinite outside the dot. Here, we keep it finite:

$$\Delta(r) = \begin{cases} 0, & r < R, \\ \Delta, & r > R, \end{cases} \tag{6.3}$$

where R is the radius of the quantum dot and Δ is an energy.

In the following sections, we will derive the eigenstates of this modified Hamiltonian and discuss the effect of an impurity with perturbation theory.

6.2 Conserved angular momentum

In order to determine the eigenstates of the Hamiltonian, we try to find a conserved quantity. With this, we can find the eigenstates of the Hamiltonian as eigenstates of this conserved quantity.

The Hamiltonian does not commute with the angular momentum operator L_z:

$$\begin{aligned}[L_z, \mathcal{H}^\tau] &= v\tau\sigma_x [L_z, q_y] - v\sigma_y [L_z, q_x] \\ &= -v\tau\sigma_x i p_x - v\sigma_y i p_y.\end{aligned} \tag{6.4}$$

Here, we used $[L_z, \Delta(r)] = 0$ because of the rotational symmetry of the quantum dot. This symmetry is specific to the circular quantum dot. An additional term is needed to conserve the total angular momentum. Analogous to Ref. [20], we define the total angular momentum operator as

$$J_z^\tau = L_z + \frac{\tau\hbar}{2}\sigma_z, \tag{6.5}$$

and find with $[\sigma_i, \sigma_j] = 2i\epsilon_{ijk}\sigma_k$:

$$\begin{aligned}\left[\frac{\tau\hbar}{2}\sigma_z, \mathcal{H}^\tau\right] &= v\tau\frac{\tau\hbar}{2}[\sigma_z, \sigma_x] q_y - v\frac{\tau\hbar}{2}[\sigma_z, \sigma_y] q_x \\ &= v\sigma_y i p_y + v\tau\sigma_x i p_x,\end{aligned} \tag{6.6}$$

such that the total angular momentum operator commutes with the Hamiltonian. Now we can find the eigenstates of the Hamiltonian as eigenstates of the total angular momentum operator.

6.3 Eigenstates of the angular momentum operator

First, we consider the angular component of the problem. As the eigenstates of the angular momentum operator do not depend on the radial component, we will use this operator to determine the form of the eigenstates.

Knowing the form of the eigenstates of L_z, we choose the ansatz

$$\psi_m^\tau(r, \theta) = \begin{pmatrix} f_m(r) e^{im\theta} \\ g_m(r) e^{in(m)\theta} \end{pmatrix}, \tag{6.7}$$

where $g_m(r)$ and $f_m(r)$ are arbitrary functions, $m \in \mathbb{Z}$ is the eigenvalue of $L_z/\hbar$ and $n(m)$ is an integer that needs to be determined. Using the eigenvalue equation of J_z^τ, we find

$$\begin{aligned}J_z^\tau \psi_m^\tau(r, \theta) &= \begin{pmatrix} L_z + \frac{\tau\hbar}{2} & 0 \\ 0 & L_z - \frac{\tau\hbar}{2} \end{pmatrix} \begin{pmatrix} f_m(r) e^{im\theta} \\ g_m(r) e^{in(m)\theta} \end{pmatrix} \\ &= \begin{pmatrix} \hbar\left(m + \frac{\tau}{2}\right) f_m(r) e^{im\theta} \\ \hbar\left(n(m) - \frac{\tau}{2}\right) g_m(r) e^{in(m)\theta} \end{pmatrix}.\end{aligned} \tag{6.8}$$

For $\psi_m^\tau(r, \theta)$ to be an eigenstate, we need to have $n(m) = m + \tau$. With that, we can express the eigenstates of the total angular momentum operator as

$$\psi_m^\tau(r, \theta) = \begin{pmatrix} f_m(r) e^{im\theta} \\ g_m(r) e^{i(m+\tau)\theta} \end{pmatrix}. \tag{6.9}$$

Considering the valley phase, the total eigenstates are given by

$$\Psi_m^\tau(r,\theta) = e^{i\boldsymbol{K}^\tau\cdot\boldsymbol{r}}\psi_m^\tau(r,\theta). \tag{6.10}$$

Next, we will derive a system of differential equations for the radial functions $f_m(r)$ and $g_m(r)$, which we will solve to find the eigenfunctions. For this, we will also introduce the boundary conditions that the radial functions need to satisfy.

6.4 The radial functions

Next, we want to find the radial functions $f_m(r)$ and $g_m(r)$ using the boundary conditions:

1. The wavefunctions have to be finite at $r = 0$.
2. The wavefunctions have to converge to zero for $r \to \infty$.
3. The wavefunctions have to be continuous at $r = R$.

With the ansatz for the eigenstates, we can write the eigenvalue equation of the Hamiltonian as

$$\mathcal{H}^\tau\psi_m^\tau(r,\theta) = E^\tau(m)\psi_m^\tau(r,\theta). \tag{6.11}$$

For the explicit form of the Hamiltonian, we find with $q_i = -i\partial_i$ and $\partial_x \pm i\partial_y = e^{\pm i\theta}(\partial_r \pm i/r\,\partial_\theta)$

$$\mathcal{H}^\tau = \begin{pmatrix} \Delta(r) & ve^{-i\tau\theta}\left(\partial_r - \frac{i\tau}{r}\partial_\theta\right) \\ -ve^{i\tau\theta}\left(\partial_r + \frac{i\tau}{r}\partial_\theta\right) & -\Delta(r) \end{pmatrix}. \tag{6.12}$$

A straightforward calculation gives us the following system of differential equations for the radial functions:

$$\begin{aligned} (E-\Delta(r))f_m(r) &= v\left(g_m'(r) + \tau\frac{m+\tau}{r}g_m(r)\right), \\ (E+\Delta(r))g_m(r) &= -v\left(f_m'(r) - \tau\frac{m}{r}f_m(r)\right). \end{aligned} \tag{6.13}$$

This system is equivalent to the following second-order differential equations:

$$\begin{aligned} 0 &= r^2f''(r) + rf'(r) + \left(\frac{r^2(E^2-\Delta^2)}{v^2} - m^2\right)f(r), \\ 0 &= r^2g''(r) + rg'(r) + \left(\frac{r^2(E^2-\Delta^2)}{v^2} - (m+\tau)^2\right)g(r). \end{aligned} \tag{6.14}$$

It is worth noting that this only holds for constant $\Delta(r)$, so a separation of domains is needed. For $r < R$, we have $\Delta(r) = 0$, and the differential equations can be expressed as:

$$\begin{aligned} 0 &= (k_Er)^2\frac{\partial^2 f}{\partial(k_Er)^2}(r) + (k_Er)\frac{\partial f}{\partial(k_Er)}(r) + \left((k_Er)^2 - m^2\right)f(r), \\ 0 &= (k_Er)^2\frac{\partial^2 g}{\partial(k_Er)^2}(r) + (k_Er)\frac{\partial g}{\partial(k_Er)}(r) + \left((k_Er)^2 - (m+\tau)^2\right)g(r), \end{aligned} \tag{6.15}$$

with $k_E^2 = E^2/v^2$. These are Bessel differential equations, and the solutions are given by linear combinations of the Bessel functions of the first and second kind $J_m(k_E r)$ and $Y_m(k_E r)$ [11]. The Bessel functions of the second kind diverge at $r = 0$, so we discard them. For $r > R$, we have $\Delta(r) = \Delta$ and, for energies $|E| < \Delta$, we can write the differential equations as

$$\begin{aligned} 0 &= (\kappa_E r)^2 \frac{\partial^2 f}{\partial(\kappa_E r)^2}(r) + (\kappa_E r)\frac{\partial f}{\partial(\kappa_E r)}(r) - \left((\kappa_E r)^2 + m^2\right) f(r), \\ 0 &= (\kappa_E r)^2 \frac{\partial^2 g}{\partial(\kappa_E r)^2}(r) + (\kappa_E r)\frac{\partial g}{\partial(\kappa_E r)}(r) - \left((\kappa_E r)^2 + (m+\tau)^2\right) g(r), \end{aligned} \tag{6.16}$$

with $\kappa_E^2 = (\Delta^2 - E^2)/v^2$. These are modified Bessel differential equations, and the solutions are given by linear combinations of the modified Bessel functions of the first and second kind $I_m(\kappa_E r)$ and $K_m(\kappa_E r)$ [11]. The modified Bessel functions of the first kind diverge for $r \to \infty$, so we discard them. The solutions are therefore given by

$$f_m(r) = \begin{cases} A_m J_m(k_E r), & r < R, \\ B_m K_m(\kappa_E r), & r > R, \end{cases} \quad g_m(r) = \begin{cases} C_m J_{m+\tau}(k_E r), & r < R, \\ D_m K_{m+\tau}(\kappa_E r), & r > R. \end{cases} \tag{6.17}$$

Using the first and second boundary conditions, we have already reduced the initial eight parameters of the radial functions to four. The remaining parameters can be determined by the continuity of the wavefunctions at $r = R$. We can reduce the parameters to one by using the third boundary condition and the differential equations Eq. (6.13), where the latter also give the spectrum. The final degree of freedom is the normalisation of the wavefunctions.

Here, k_E and κ_E are the wavevectors inside and outside the quantum dot, respectively. We only consider the case $|E| < \Delta$, such that the wavevectors are real and the Bessel functions chosen only deal with real arguments. Additionally, we choose the wavevectors to be positive with $k_E = |E|/v$ and $\kappa_E = \sqrt{\Delta^2 - E^2}/v$, such that the Bessel functions are well defined.

In the next section, we will use the result for the radial functions to determine the spectrum of the Hamiltonian and the eigenstates of the quantum dot.

6.5 Spectrum of the Hamiltonian

We now want to find the spectrum of the Hamiltonian. In order to do that, we use the differential equations Eq. (6.13) to express the parameters C_m and D_m in terms of A_m and B_m. After short calculations using the derivative relations of the Bessel functions [11], we find

$$\begin{aligned} C_m &= \tau \frac{E}{v k_E} A_m = \tau \,\mathrm{sgn}(E) A_m, \\ D_m &= \frac{\Delta - E}{v \kappa_E} B_m = \sqrt{\frac{\Delta - E}{\Delta + E}} B_m. \end{aligned} \tag{6.18}$$

Additionally, we can use the continuity of the wavefunctions at $r = R$ to express B_m in terms of A_m and D_m in terms of C_m:

$$\begin{aligned} B_m &= A_m \frac{J_m(k_E R)}{K_m(\kappa_E R)}, \\ D_m &= C_m \frac{J_{m+\tau}(k_E R)}{K_{m+\tau}(\kappa_E R)}. \end{aligned} \tag{6.19}$$

Using the relations for C_m and D_m, we can express the latter as

$$B_m = A_m \tau \operatorname{sgn}(E) \sqrt{\frac{\Delta + E}{\Delta - E}} \frac{J_{m+\tau}(k_E R)}{K_{m+\tau}(\kappa_E R)}. \tag{6.20}$$

Combining the two expressions for B_m, we find the following equation for the spectrum of the Hamiltonian:

$$\frac{J_m(k_E R)}{K_m(\kappa_E R)} = \tau \operatorname{sgn}(E) \sqrt{\frac{\Delta + E}{\Delta - E}} \frac{J_{m+\tau}(k_E R)}{K_{m+\tau}(\kappa_E R)}. \tag{6.21}$$

For a fixed (m, τ), Eq. (6.21) is a transcendental equation with a finite number of solutions for the energy E with $E^2 < \Delta^2$, which we label by $n \in \mathbb{N}$. The solutions are denoted as $E^\tau_{n,m}$, and the corresponding eigenstates are denoted as $\psi^{\tau,n}_m(r, \theta)$. The radial functions can be expressed as

$$\begin{aligned} f^\tau_{n,m}(r) &= \begin{cases} A^\tau_{n,m} J_m(k^\tau_{n,m} r), & r < R, \\ A^\tau_{n,m} \frac{J_m(k^\tau_{n,m} R)}{K_m(\kappa^\tau_{n,m} R)} K_m(\kappa^\tau_{n,m} r), & r > R, \end{cases} \\ g^\tau_{n,m}(r) &= \begin{cases} \tau A^\tau_{n,m} \operatorname{sgn}(E^\tau_{n,m}) J_{m+\tau}(k^\tau_{n,m} r), & r < R, \\ \tau A^\tau_{n,m} \operatorname{sgn}(E^\tau_{n,m}) \frac{J_{m+\tau}(k^\tau_{n,m} R)}{K_{m+\tau}(\kappa^\tau_{n,m} R)} K_{m+\tau}(\kappa^\tau_{n,m} r), & r > R. \end{cases} \end{aligned} \tag{6.22}$$

Changing the valley index $\tau \to -\tau$ at constant energy E yields the following equation

$$\begin{aligned} \frac{J_m(k^{-\tau}_{n,m} R)}{K_m(\kappa^{-\tau}_{n,m} R)} &= -\tau \operatorname{sgn}(E^{-\tau}_{n,m}) \sqrt{\frac{\Delta + E^{-\tau}_{n,m}}{\Delta - E^{-\tau}_{n,m}}} \frac{J_{m-\tau}(k^{-\tau}_{n,m} R)}{K_{m-\tau}(\kappa^{-\tau}_{n,m} R)} \\ \frac{(-1)^{-m} J_{-m}(k^{-\tau}_{n,m} R)}{K_{-m}(\kappa^{-\tau}_{n,m} R)} &= -\tau \operatorname{sgn}(E^{-\tau}_{n,m}) \sqrt{\frac{\Delta + E^{-\tau}_{n,m}}{\Delta - E^{-\tau}_{n,m}}} \frac{(-1)^{-m+\tau} J_{-m+\tau}(k^{-\tau}_{n,m} R)}{K_{-m+\tau}(\kappa^{-\tau}_{n,m} R)} \\ \frac{J_{-m}(k^{-\tau}_{n,m} R)}{K_{-m}(\kappa^{-\tau}_{n,m} R)} &= \tau \operatorname{sgn}(E^{-\tau}_{n,m}) \sqrt{\frac{\Delta + E^{-\tau}_{n,m}}{\Delta - E^{-\tau}_{n,m}}} \frac{J_{-m+\tau}(k^{-\tau}_{n,m} R)}{K_{-m+\tau}(\kappa^{-\tau}_{n,m} R)}, \end{aligned} \tag{6.23}$$

so $E^\tau_{n,m} = E^{-\tau}_{n,-m}$. Switching the valley at constant energy E switches the angular momentum $m \to -m$ and the total angular momentum $j = m + \tau/2 \to -j$. Thus, the eigenstates of the Hamiltonian are now the complex conjugates up to the overall sign $(-1)^m$. As the valley swap has the effect of a time reversal on the Hamiltonian, these degenerate eigenstates are related by time-reversal symmetry.

For the following discussion, we collapse the notation with $\nu = (n, m, \tau)$ and $\nu^- = (n, -m, -\tau)$ and write

$$\begin{aligned} A^\tau_{n,m} &= A_\nu, & J_m(k^\tau_{n,m} r) &= j_\nu(r), & K_m(\kappa^\tau_{n,m} r) &= k_\nu(r), \\ E^\tau_{n,m} &= E_\nu, & J_{m+\tau}(k^\tau_{n,m} r) &= j_{\nu+\tau}(r), & K_{m+\tau}(\kappa^\tau_{n,m} r) &= k_{\nu+\tau}(r). \end{aligned}$$

Using this notation, we will now discuss the effect of an impurity on the eigenstates of the Hamiltonian. For this, we will use degenerate perturbation theory.

6.6 Perturbation theory for an impurity

For this section, it is important to note that the wavefunctions are only defined on lattice sites. The 2D-vector form with a position vector $\boldsymbol{r}$ as an argument as in Eq. (6.7) is only a convenient

representation. In fact, the wavefunctions have the discrete form

$$\psi = \sum_i \psi^{\alpha_i}(\boldsymbol{r}_i)\boldsymbol{s}_i, \tag{6.24}$$

where $\psi^{\alpha_i}(\boldsymbol{r}_i)$ is the notation of the previous chapters, $\boldsymbol{s}_i$ is the orthonormal basis element describing the state at r_i and $\alpha_i \in \{A, B\}$ is the sublattice of the lattice site. Evaluating the wavefunctions at a site also means dropping the 2D-vector form; hence, the index α is dropped in the following.

In the presence of an impurity, the system is perturbed and the Hamiltonian is modified with $\mathcal{H} = \mathcal{H}_0 + V$, where $\mathcal{H}_0$ is the unperturbed Hamiltonian and V is the potential created by the impurity. However, the eigenenergies of the Hamiltonian are discrete for $E^2 < \Delta^2$, so the Lippmann-Schwinger ansatz as before does not converge. As stated above, the eigenstates in the set $D = \{\Psi_\nu, \Psi_{\nu^-}\}$ are degenerate, so we can use degenerate perturbation theory to find the perturbed eigenstates [9]. The perturbation is given analogously to Chapter 5 by

$$V = V_0 P(\boldsymbol{r}_0). \tag{6.25}$$

We define the matrix M as V in the basis D:

$$M = V_0 \begin{pmatrix} |\Psi_\nu(\boldsymbol{r}_0)|^2 & (\Psi_\nu(\boldsymbol{r}_0))^* \Psi_{\nu^-}(\boldsymbol{r}_0) \\ (\Psi_{\nu^-}(\boldsymbol{r}_0))^* \Psi_\nu(\boldsymbol{r}_0) & |\Psi_{\nu^-}(\boldsymbol{r}_0)|^2 \end{pmatrix}. \tag{6.26}$$

We find the energy corrections as the eigenvalues of M with the corresponding eigenvectors

$$\begin{aligned} &\epsilon_0 = 0, && \epsilon_1 = V_0 \left(|\Psi_\nu(\boldsymbol{r}_0)|^2 + |\Psi_{\nu^-}(\boldsymbol{r}_0)|^2 \right) \\ &\Phi_0^{(0)} = \frac{1}{\|\Psi\|} \begin{pmatrix} \Psi_{\nu^-}(\boldsymbol{r}_0) \\ -\Psi_\nu(\boldsymbol{r}_0) \end{pmatrix}, && \Phi_1^{(0)} = \frac{1}{\|\Psi\|} \begin{pmatrix} (\Psi_\nu(\boldsymbol{r}_0))^* \\ (\Psi_{\nu^-}(\boldsymbol{r}_0))^* \end{pmatrix}, \end{aligned} \tag{6.27}$$

with $\|\Psi\|^2 = |\Psi_\nu(\boldsymbol{r}_0)|^2 + |\Psi_{\nu^-}(\boldsymbol{r}_0)|^2$. The first-order corrections are given by

$$\Phi_i^{(1)} = \sum_{\mu \notin D} \frac{\langle q, V\Phi_i^{(0)} \rangle}{E_\nu - E_\mu} q, \tag{6.28}$$

where $q = \Psi_\mu$ are the eigenstates of the unperturbed Hamiltonian $\mathcal{H}_0$ with eigenenergies E_q, $\langle q, V\Phi_i^{(0)} \rangle$ is the scalar product of q and $V\Phi_i^{(0)}$ on the position space, and $\nu = (n, m, \tau)$ is the index of the eigenenergy of the degenerate states. We thus find

$$\Phi_0^{(1)} = 0, \quad \Phi_1^{(1)} = V_0 \|\Psi\| \sum_{\mu \notin D} \frac{(q(\boldsymbol{r}_0))^*}{E_\nu - E_\mu} q. \tag{6.29}$$

For an A-site impurity within the quantum dot, we find

$$\Psi_\nu(\boldsymbol{r}_0) = e^{i\boldsymbol{K}^\tau \cdot \boldsymbol{r}_0 + im\theta_0} A_\nu j_\nu(r_0). \tag{6.30}$$

We write $\|\Psi_\nu^A\|^2 = 2|A_\nu j_\nu(r_0)|^2$, where we used $J_{-m} = (-1)^m J_m$, $K_{-m} = K_m$ [11] and thus $|A_{\nu^-}| = |A_\nu|$. We obtain the following first-order corrections:

$$\begin{aligned} &\epsilon_0 = 0, && \Phi_0^{(1)} = 0, \\ &\epsilon_1 = V_0 \, \|\Psi_\nu^A\|^2, && \Phi_1^{(1)} = V_0 \, \|\Psi_\nu^A\| \sum_{\mu \notin D} \frac{(\Psi_\mu(\boldsymbol{r}_0))^*}{E_\nu - E_\mu} \Psi_\mu. \end{aligned} \tag{6.31}$$

Analogously, for a B-site impurity, we find

$$\Psi_\nu(\boldsymbol{r}_0) = e^{i\boldsymbol{K}^\tau\cdot\boldsymbol{r}_0+i(m+\tau)\theta_0}\tau\,\mathrm{sgn}(E_\nu)A_\nu j_{\nu+\tau}(r_0), \tag{6.32}$$

and with $\|\Psi_\nu^B\|^2 = 2|A_\nu j_{\nu+\tau}(r_0)|^2$

$$\begin{aligned} &\epsilon_0 = 0, && \Phi_0^{(1)} = 0, \\ &\epsilon_1 = V_0\,\|\Psi_\nu^B\|^2, && \Phi_1^{(1)} = V_0\,\|\Psi_\nu^B\| \sum_{\mu\notin D} \frac{(\Psi_\mu(\boldsymbol{r}_0))^*}{E_\nu - E_\mu}\,\Psi_\mu. \end{aligned} \tag{6.33}$$

For the $V_0 \to \infty$ limit, the correction ϵ_1 diverges. However, $\epsilon_0 = 0$ for all values of V_0. That also means that $V\Phi_0 = 0$, so that Φ_0 is an exact eigenstate of the perturbed Hamiltonian. This eigenstate completely mixes the degenerate states Ψ_ν and Ψ_{ν^-} and, with that, the valleys. This result is similar to the result of Chapter 5, where the scattered wave also describes a full intervalley mixing.

Chapter 7

Conclusion and outlook

In this thesis, we have studied the low-energy scattering off single-site impurities in graphene and the effect of an impurity in a graphene quantum dot.

We used the tight-binding model of the honeycomb lattice and linearised the Hamiltonian around the two Dirac points $\boldsymbol{K}$ and $\boldsymbol{K}'$. With this Dirac Hamiltonian, the Green's function was derived analytically. The result is a matrix of Hankel functions for each valley, where the two valleys are related by $G_0^-(\theta) = G_0^+(-\theta)$. Using this result, we formulated an expression for the total Green's function in a low-energy and far-field approximation.

We used numerical integration over the Brillouin zone to verify that our approximation describes the Green's function well for large r but fails at small r. At $r = 0$, the Dirac Green's function diverges, and a result controlling this divergence was derived. For this, we calculated the exact analytical value $G_0^{AA}(0; z)$ by relating it to the triangular lattice Green's function of Horiguchi [12]. This value is finite and additionally served as a test for the numerical integration.

We then combined these results into a Green's function with the exact value at $r = 0$ and the far-field approximation for $r > 0$. This result does not rely on any numerical evaluation to control the divergence at $r = 0$.

Using this Green's function, we solved the Lippmann-Schwinger equation for a single impurity. With the far-field solution, we determined the resulting cross section

$$\sigma = \frac{V_0^2 |R|^2 k_E A_{\text{cell}}^2}{v^2}.$$

It is isotropic, independent of the valley index τ and does not depend on the incoming direction φ of a plane wave. Additionally, the impurity mixes both valleys equally, which is expected for a delta potential. Furthermore, the low-energy limit of our exact result agrees with the result of Basko [6]. The parameter $e^\gamma r_0 = a$, which Basko determined numerically, follows analytically from our result. With the cross section, we estimated the conductivity for a density n of vacancies, i.e. impurities with $V_0 \to \infty$,

$$\sigma_{\text{el}} = \frac{2e^2}{\hbar\pi} \frac{v^2 |G_0^{AA}(0; E_F)|^2}{n A_{\text{cell}}^2}.$$

It contains no free parameter. Apart from the density of vacancies, it only depends on the exact

Green's function at zero distance at the Fermi energy. When written in terms of the number of vacancies per unit cell, nA_{cell}, the lattice constant also drops out.

Lastly, we considered a circular graphene quantum dot. We defined it by a mass term $\Delta(r)\sigma_z$. As L_z alone does not commute with the Hamiltonian, we introduced the total angular momentum $J_z^\tau = L_z + \tau\hbar\sigma_z/2$. We found the eigenstates as simultaneous eigenfunctions of J_z^τ and the Hamiltonian and derived the spectrum. For $|E| < \Delta$, the spectrum is discrete and twofold degenerate. The degenerate pairs consist of states in opposite valleys. As the Lippmann-Schwinger equation is not applicable to a discrete spectrum, we used degenerate perturbation theory to determine the effect of a single-site impurity. For an impurity strength V_0, one of the degenerate states stays at the same energy, while the other state is shifted by $\epsilon_1 = V_0\|\Psi\|^2$. The unshifted state is an exact solution for any V_0. It is a superposition of the two valley states. In both the plain graphene sheet and the quantum dot, the single-site impurity mixes the valleys completely.

As an outlook, the methods of this thesis can be applied to impurities in different geometries. With the same mass term, a channel of width h can be defined by $\Delta(y) = 0$ for $|y| < h/2$ and $\Delta(y) = \Delta$ otherwise. In contrast to the quantum dot, the spectrum along the channel is continuous. Thus, the scattering off an impurity inside the channel could again be described with the Lippmann-Schwinger equation, now with the Green's function of the channel. Joining two quantum dots by such a channel gives a double dot with an impurity in the channel, where it would be interesting to see how the impurity affects the coupling between the two dots.

Furthermore, only impurities on a single site were considered. For an impurity extending over more than one site, e.g. a two-site impurity, the potential is no longer constant in momentum space. The scattering amplitude is then expected to depend on θ.

Appendix A

Deriving the relation to the Horiguchi result

This appendix shows the calculation that leads to Eq. (4.3).

A.1 Ansatz for G_0

With $G_0 = (z - \mathcal{H}_0)^{-1}$, we can simply invert the 2×2 matrix

$$\begin{aligned} G_0 &= \begin{pmatrix} z & tf(\boldsymbol{k}) \\ tf^*(\boldsymbol{k}) & z \end{pmatrix}^{-1} = \frac{1}{z^2 - t^2|f(\boldsymbol{k})|^2} \begin{pmatrix} z & -tf(\boldsymbol{k}) \\ -tf^*(\boldsymbol{k}) & z \end{pmatrix} \\ G_0(\boldsymbol{r}) &= \frac{A_{\text{cell}}}{(2\pi)^2} \int_{\text{BZ}} \mathrm{d}^2\boldsymbol{k} \frac{1}{z^2 - t^2|f(\boldsymbol{k})|^2} \begin{pmatrix} z & -tf(\boldsymbol{k}) \\ -tf^*(\boldsymbol{k}) & z \end{pmatrix} e^{i\boldsymbol{k}\cdot\boldsymbol{r}}. \end{aligned} \tag{A.1}$$

A.2 Rewriting $|f(\boldsymbol{k})|^2$ and determining the integral boundaries

With $f(\boldsymbol{k}) = \sum_{\boldsymbol{\delta}_i} e^{-i\boldsymbol{k}\cdot\boldsymbol{\delta}_i}$, we write

$$\begin{aligned} |f(\boldsymbol{k})|^2 &= \sum_{\boldsymbol{\delta}_i, \boldsymbol{\delta}_j} e^{-i\boldsymbol{k}\cdot(\boldsymbol{\delta}_i - \boldsymbol{\delta}_j)} \\ &= 3 + 2\left[\cos(\boldsymbol{k}\cdot(\boldsymbol{\delta}_1 - \boldsymbol{\delta}_2)) + \cos(\boldsymbol{k}\cdot(\boldsymbol{\delta}_1 - \boldsymbol{\delta}_3)) + \cos(\boldsymbol{k}\cdot(\boldsymbol{\delta}_2 - \boldsymbol{\delta}_3))\right] \\ &= 3 + 4\cos\left(\frac{\boldsymbol{k}\cdot(\boldsymbol{a}_1 + \boldsymbol{a}_2)}{2}\right)\cos\left(\frac{\boldsymbol{k}\cdot(\boldsymbol{a}_1 - \boldsymbol{a}_2)}{2}\right) + 2\cos(\boldsymbol{k}\cdot(\boldsymbol{a}_1 - \boldsymbol{a}_2)) \\ &= 3 + 4\cos\left(\frac{3a}{2}k_x\right)\cos\left(\frac{\sqrt{3}a}{2}k_y\right) + 2\cos(\sqrt{3}ak_y). \end{aligned} \tag{A.2}$$

Now we consider the integral boundaries. For this, we sketch the Brillouin zone in Fig. A.1. For the self-consistency condition, only $G_0^{AA}(0)$ and $G_0^{BB}(0)$ are needed. As $G_0^{AA}(0) = G_0^{BB}(0)$,

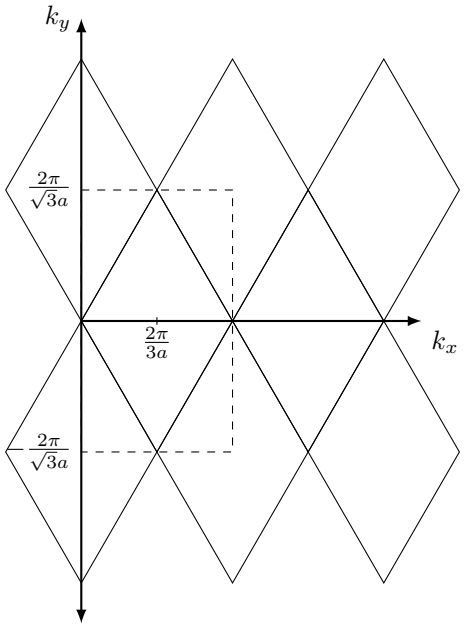


Figure A.1: A sketch of the Brillouin zones. Each diamond represents a whole Brillouin zone. The area surrounded by the dashed lines thus includes two Brillouin zones. The diamonds are spanned by the reciprocal lattice vectors $\boldsymbol{b}_1 = 2\pi/3a\big(1, \sqrt{3}\big)$ and $\boldsymbol{b}_2 = 2\pi/3a\big(1, -\sqrt{3}\big)$.

we calculate

$$G_0^{AA}(0) = \frac{A_{\text{cell}}}{(2\pi)^2}\frac{1}{2}\int_0^{\frac{4\pi}{3a}} \mathrm{d}k_x \int_{-\frac{2\pi}{\sqrt{3}a}}^{\frac{2\pi}{\sqrt{3}a}} \mathrm{d}k_y \frac{z}{z^2 - t^2\left(3 + 4\cos\left(\frac{3a}{2}k_x\right)\cos\left(\frac{\sqrt{3}a}{2}k_y\right) + 2\cos(\sqrt{3}ak_y)\right)}. \tag{A.3}$$

A.3 Transforming the integral and finding the expression

With $w = z/t$, $A = a/2$ and $B = \sqrt{3}a/2$, the equation becomes

$$G_0^{AA}(0) = \frac{1}{2t^2}\frac{A_{\text{cell}}}{(2\pi)^2}\int_0^{\frac{2\pi}{3A}} \mathrm{d}k_x \int_{-\frac{\pi}{B}}^{\frac{\pi}{B}} \mathrm{d}k_y \frac{z}{(w^2-3) - 2\cos(2Bk_y) - 4\cos(3Ak_x)\cos(Bk_y)}. \tag{A.4}$$

Since the integrand is periodic with period $2\pi/3A$, we triple the area and transform the boundaries to obtain

$$G_0^{AA}(0) = \frac{1}{6t^2}\frac{A_{\text{cell}}}{(2\pi)^2}\int_{-\frac{\pi}{A}}^{\frac{\pi}{A}} \mathrm{d}k_x \int_{-\frac{\pi}{B}}^{\frac{\pi}{B}} \mathrm{d}k_y \frac{z}{(w^2-3) - 2\cos(2Bk_y) - 4\cos(3Ak_x)\cos(Bk_y)} \tag{A.5}$$

and, using $A_{\text{cell}} = \frac{3\sqrt{3}}{2}a^2$, we obtain the form

$$G_0^{AA}(0) = \frac{1}{2t} 2w \frac{AB}{(2\pi)^2} \int_{-\frac{\pi}{A}}^{\frac{\pi}{A}} \mathrm{d}k_x \int_{-\frac{\pi}{B}}^{\frac{\pi}{B}} \mathrm{d}k_y \frac{1}{(w^2-3) - 2\cos(2Bk_y) - 4\cos(3Ak_x)\cos(Bk_y)}. \quad \text{(A.6)}$$

We can now compare this to Horiguchi's result [12], which is given by

$$G_{\mathrm{H}}^{AA}(0,0) = 4t_H \frac{ab}{(2\pi)^2} \int_{-\frac{\pi}{a}}^{\frac{\pi}{a}} \mathrm{d}x \int_{-\frac{\pi}{b}}^{\frac{\pi}{b}} \mathrm{d}y \frac{1}{4t_H^2 - 3 - 2\cos(2ax) - 4\cos(3by)\cos(ay)}, \quad \text{(A.7)}$$

we see that

$$G_0^{AA}(0) = \frac{1}{2t} G_{\mathrm{H}}^{AA}(0,0), \quad \text{(A.8)}$$

with the identifications $a = B$, $b = A$ and $t_H = w/2$.

Appendix B

Comparison to the Basko result

This appendix shows that the result of Basko [6] can be derived analytically using the results of this thesis. The index B is used to denote the results of Basko. Our cross section is of the form

$$\sigma = \frac{V_0^2 |R|^2 |E| A_{\text{cell}}^2}{v^3}, \tag{B.1}$$

where $R = \frac{1}{\sqrt{2}(1 - V_0 G_0^{AA}(0;E))}$. Basko [6] obtained the total cross section, averaged over the impurity positions,

$$\sigma_B = \frac{\pi^2 v |E|/2}{\left(\frac{\pi v^2}{V_0 A_{\text{cell}}} + E \ln\left(\frac{2v}{e^\gamma r_0 |E|}\right)\right)^2 + \left(\frac{\pi E}{2}\right)^2}. \tag{B.2}$$

With

$$|T_0|^2 = \frac{\pi^2 v^4}{A_{\text{cell}}^2} \frac{1}{\left(\frac{\pi v^2}{V_0 A_{\text{cell}}} + E \ln\left(\frac{2v}{e^\gamma r_0 |E|}\right)\right)^2 + \left(\frac{\pi E}{2}\right)^2}, \tag{B.3}$$

we can write

$$\sigma_B = \frac{A_{\text{cell}}^2 |T_0|^2 |E|}{2v^3}. \tag{B.4}$$

For the results to be equivalent, we need $|T_0|^2 = 2V_0^2 |R|^2$. This holds if

$$T_0^{-1} = \frac{1}{V_0} - G_{B,0}^{AA}(0;E) = (\sqrt{2} V_0 R)^{-1} = \frac{1}{V_0} - G_0^{AA}(0;E). \tag{B.5}$$

The above equation shows that the two results are equivalent under the condition that the Green's functions at zero distance are equivalent. We now approximate $G_0^{AA}(0;E) = \frac{1}{4t}\frac{w}{\pi} g K(k^2)$ for low energies $w \ll 1$, where $K(k^2)$ is taken on the branch Eq. (4.7). For $w \to 0$, we have

$$g \sim \frac{8i}{\sqrt{3}}, \qquad k^2 \sim -\frac{16w}{3}. \tag{B.6}$$

For $k^2 \to 0$, we use $K(k^2) \sim \pi/2$ and $K(1-k^2) \sim \frac{1}{2}\ln(16/k^2)$ [11]. With $z = E + i0$, the argument $16/k^2 \sim -3/w$ lies just above the negative real axis, so that $K(1-k^2) \sim \frac{1}{2}\ln\left(\frac{3}{w}\right) + \frac{i\pi}{2}$. The branch Eq. (4.7) then gives

$$K(k^2) + 2i\, K(1-k^2) \sim i \ln\left(\frac{3}{w}\right) - \frac{\pi}{2}. \tag{B.7}$$

This yields

$$G_0^{AA}(0;E) \sim -\frac{2E}{\sqrt{3}t^2\pi}\left(\ln\left(\frac{3t}{E}\right)+\frac{i\pi}{2}\right), \tag{B.8}$$

where we already used $w = E/t$. Basko's result for the Green's function is

$$G_{B,0}^{AA}(0;E) \sim -\frac{A_{\text{cell}}E}{\pi v^2}\left(\ln\left(\frac{2v}{e^\gamma r_0|E|}\right)+\frac{i\pi}{2}\right), \tag{B.9}$$

where γ is the Euler-Mascheroni constant and r_0 is a length of the order of the size of the impurity. Its value was determined by numerical integration over the whole first Brillouin zone, which gives $e^\gamma r_0 = a$. With

$$\frac{A_{\text{cell}}}{v^2} = \frac{\sqrt{27}a^2}{2(\frac{3at}{2})^2} = \frac{2}{\sqrt{3}t^2} \tag{B.10}$$

and

$$3t = \frac{2v}{a}, \tag{B.11}$$

we find that the low-energy limit of our analytical result agrees with Basko's result exactly for $e^\gamma r_0 = a$, confirming the numerical result.

We thus have the low-energy limit of the Green's function in the form

$$G_0^{AA}(0;E) \sim -\frac{A_{\text{cell}}E}{\pi v^2}\left(\ln\left(\frac{2v}{aE}\right)+\frac{i\pi}{2}\right). \tag{B.12}$$

Bibliography

[1] K. S. Novoselov, A. K. Geim, S. V. Morozov, D. Jiang, Y. Zhang, S. V. Dubonos, et al. "Electric Field Effect in Atomically Thin Carbon Films". In: *Science* 306.5696 (2004), pp. 666–669. DOI: 10.1126/science.1102896.

[2] A. H. Castro Neto, F. Guinea, N. M. R. Peres, K. S. Novoselov, and A. K. Geim. "The electronic properties of graphene". In: *Rev. Mod. Phys.* 81 (1 Jan. 2009), pp. 109–162. DOI: 10.1103/RevModPhys.81.109.

[3] N. M. R. Peres, F. Guinea, and A. H. Castro Neto. "Electronic properties of disordered two-dimensional carbon". In: *Phys. Rev. B* 73.12 (2006), p. 125411. DOI: 10.1103/PhysRevB.73.125411.

[4] S. Das Sarma, S. Adam, E. H. Hwang, and E. Rossi. "Electronic transport in two-dimensional graphene". In: *Rev. Mod. Phys.* 83.2 (2011), pp. 407–470. DOI: 10.1103/RevModPhys.83.407.

[5] V. M. Pereira, J. M. B. Lopes dos Santos, and A. H. Castro Neto. "Modeling disorder in graphene". In: *Phys. Rev. B* 77.11 (2008), p. 115109. DOI: 10.1103/PhysRevB.77.115109.

[6] D. M. Basko. "Resonant low-energy electron scattering on short-range impurities in graphene". In: *Phys. Rev. B* 78 (11 Sept. 2008), p. 115432. DOI: 10.1103/PhysRevB.78.115432.

[7] P. R. Wallace. "The Band Theory of Graphite". In: *Phys. Rev.* 71.9 (1947), pp. 622–634. DOI: 10.1103/PhysRev.71.622.

[8] C. Bena and G. Montambaux. "Remarks on the tight-binding model of graphene". In: *New J. Phys.* 11.9 (2009), p. 095003. DOI: 10.1088/1367-2630/11/9/095003.

[9] J. J. Sakurai and J. Napolitano. *Modern Quantum Mechanics*. 3rd ed. Cambridge: Cambridge University Press, 2020. DOI: 10.1017/9781108587280.

[10] E. N. Economou. *Green's Functions in Quantum Physics*. 3rd ed. Berlin, Heidelberg: Springer, 2006. DOI: 10.1007/3-540-28841-4.

[11] *NIST Digital Library of Mathematical Functions*. Accessed: 08-08-2026. URL: https://dlmf.nist.gov/.

[12] T. Horiguchi. "Lattice Green's Functions for the Triangular and Honeycomb Lattices". In: *Journal of Mathematical Physics* 13.9 (1972), pp. 1411–1419. DOI: 10.1063/1.1666155.

[13] S. K. Adhikari. "Quantum scattering in two dimensions". In: *Am. J. Phys.* 54.4 (1986), pp. 362–367. DOI: 10.1119/1.14623.

[14] V. M. Pereira, F. Guinea, J. M. B. Lopes dos Santos, N. M. R. Peres, and A. H. Castro Neto. "Disorder Induced Localized States in Graphene". In: *Phys. Rev. Lett.* 96.3 (2006), p. 036801. DOI: 10.1103/PhysRevLett.96.036801.

[15] T. Stauber, N. M. R. Peres, and F. Guinea. "Electronic transport in graphene: A semi-classical approach including midgap states". In: *Phys. Rev. B* 76.20 (2007), p. 205423. DOI: 10.1103/PhysRevB.76.205423.

[16] P. M. Ostrovsky, I. V. Gornyi, and A. D. Mirlin. "Electron transport in disordered graphene". In: *Phys. Rev. B* 74.23 (2006), p. 235443. DOI: 10.1103/PhysRevB.74.235443.

[17] T. O. Wehling, S. Yuan, A. I. Lichtenstein, A. K. Geim, and M. I. Katsnelson. "Resonant Scattering by Realistic Impurities in Graphene". In: *Phys. Rev. Lett.* 105.5 (2010), p. 056802. DOI: 10.1103/PhysRevLett.105.056802.

[18] J.-H. Chen, W. G. Cullen, C. Jang, M. S. Fuhrer, and E. D. Williams. "Defect Scattering in Graphene". In: *Phys. Rev. Lett.* 102.23 (2009), p. 236805. DOI: 10.1103/PhysRevLett.102.236805.

[19] M. V. Berry and R. J. Mondragon. "Neutrino billiards: time-reversal symmetry-breaking without magnetic fields". In: *Proc. R. Soc. Lond. A* 412.1842 (1987), pp. 53–74. DOI: 10.1098/rspa.1987.0080.

[20] S. Schnez, K. Ensslin, M. Sigrist, and T. Ihn. "Analytic model of the energy spectrum of a graphene quantum dot in a perpendicular magnetic field". In: *Phys. Rev. B* 78.19 (2008), p. 195427. DOI: 10.1103/PhysRevB.78.195427.

Acknowledgements

First of all, I would like to thank Professor Fabian Hassler for giving me the opportunity to work on this project. His guidance has been essential for my undestanding and progress throughout this thesis.

I also want to thank Konstantinos Kontogeorgiou, my supervisor and advisor throughout this project, who was always available to answer my questions whenever I was stuck.

Additionally, I would like to thank everyone in the Group for their support and discussions, especially regarding the presentation and the notation for partial derivatives. I would also like to thank my fellow students for the time we spend together puzzling over how we are going to disappoint our supervisors this time.

Finally, I would like to thank my family and friends for their support throughout this project.

Declaration on the use of AI tools

In this thesis, AI tools were used to assist in writing the Python scripts for the numerical calculations. Furthermore, AI tools were used to check the thesis for spelling and grammar errors, to double-check calculations and derivations, to search for literature and to double-check the cited references against their sources.